To the Graduate Council:

I am submitting herewith a thesis written by S. Babu entitled "Transient Thermal Analysis of a High Power Density Magnetohydrodynamic Nozzle". I have examined the final copy of this thesis for form and content and recommend that it be accepted in partial fulfillment of the requirements for the degree of Master of Science, with a major in Mechanical Engineering.

Harold J. Schmidt, Major Professor

We have read this thesis
and recommend its acceptance:

Accepted for the Council:

Vice Provost
and Dean of The Graduate School

STATEMENT OF PERMISSION TO USE

In presenting this thesis in partial fulfillment of the requirements for a Master's degree at The University of Tennessee, Knoxville, I agree that the Library shall make it available to borrowers under rules of the Library. Brief quotations from this thesis are allowable without special permission, provided that accurate acknowledgment of the source is made.

Permission for extensive quotation from or reproduction of this thesis may be granted by my major professor, or in his absence, by the Head of Interlibrary Services when, in the opinion of either, the proposed use of the material is for scholarly purposes. Any copying or use of the material in this thesis for financial gain shall not be allowed without my written permission.

Signature Bal

Date 11/29/90

TRANSIENT THERMAL ANALYSIS OF A HIGH POWER DENSITY MAGNETOHYDRODYNAMIC NOZZLE

A Thesis

Presented for the

Master of Science

Degree

The University of Tennessee, Knoxville

S. Babu

December 1990

DEDICATION

This thesis is dedicated to my parents

Mr. Appurajapuram Krishnamurthy Sethuraman
(திரு. அப்புராஜபுரம் கிருஷ்ணமூர்த்தி சேதுராமன்)

and

Mrs. Nagalakshmi Sethuraman
(திருமதி. நாகலக்ஷ்மி சேதுராமன்)

who have given me invaluable educational opportunities.

ACKNOWLEDGMENTS

I am greatly indebted to Dr. Harold J. Schmidt, chairman of my thesis committee, for his supervision and guidance throughout the development of this thesis. His patience and support during this time are greatly appreciated.

I also wish to extend my sincerest thanks to Mr. John T. Lineberry and Dr. James N. Chapman for their valuable suggestions and assistance in improving my thesis.

Finally, I would like to thank Dr. Schmidt and Mr. Lineberry for permission to use the data and descriptive background material for the experimental test program at UTSI.

ABSTRACT

The transient heat conduction in a high power density magnetohydrodynamic nozzle has been numerically modeled. The numerical scheme is based on finite differences and the solution procedure used a successive under relaxation technique. The comparisons of numerical results with analytical solutions for simpler problems and with the available experimental data show good agreement. The numerical model also inferred additional data that could not be obtained through the experiments. This information and the implications of the results on the future design of similar components are also discussed.

TABLE OF CONTENTS

CHAPTER PAGE

1. INTRODUCTION 1
2. ANALYSIS 6
    2.1 Experimental Set-up 6
    2.2 Numerical Modeling 13
        2.2.1 Problem Formulation 13
        2.2.2 Finite Differences 21
        2.2.3 Boundary Conditions 21
        2.2.4 Finite Difference Equations 22
        2.2.5 Solution Procedure 23
3. RESULTS 25
    3.1 Comparison of Numerical Analytical Solutions 25
    3.2 Experiments and Data 27
        3.2.1 Experiments 27
        3.2.2 Combustion Test Data 30
    3.3 Comparison of Numerical Results and Experimental Data . . 36
        3.3.1 The Comparison 36
        3.3.2 Error Analysis 40
        3.3.3 Explanations for Deviations 44
        3.3.4 Nozzle Inner Face Temperatures 46
        3.3.5 Two Dimensional Nature of Solutions 50
4. CONCLUSIONS 53
LIST OF REFERENCES 54

APPENDICES 56
APPENDIX A. Derivatives in the Computational Plane . . . 57
APPENDIX B. Finite Difference Approximations
in the Computational Plane 58
APPENDIX C. Finite Difference Forms of Boundary Conditions 61
VITA 63

LIST OF FIGURES

FIGURE PAGE

2.1 Experimental Set-up 7
2.2 Combustor-Nozzle System 9
2.3 Schematic of Idealized Nozzle Geometry 15
2.4 Numerical Grid in the Physical and Computational Planes 18
3.1 Geometry and Problem in the Case of a Straight Cylindrical Duct 26
3.2 Comparison of Numerical and Analytical Solutions[3], Straight Cylindrical Duct, Uniform and Constant Heat Flux: a) Heating Curves, b) Equlibrating Curves 28
3.3 Typical Combustor Pressure Data Showing Event Times 31
3.4 Typical Nozzle Temperature Transients Following a Firing (Test Run #10) 35
3.5 Typical Heat Flux Distribution Chosen for Numerical Calculations (Run #35) 39
3.6 Nozzle Temperature Transients for Run #35 over 1000 Seconds Following Ignition 39
3.7 Comparison of Numerical and Experimental Temperature Transients, Run #35 41
3.8 Comparison of Numerical and Experimental Temperature Transients, Run #32 42
3.9 Comparison of Numerical and Experimental Temperature Transients, Run #28 43

3.10 Comparison of Heat Input and the Change
in Heat Stored, Run #35 45
3.11 Nozzle Inner Face Temperature Transients, Run #35 48
3.12 Time History of Isotherms in the Nozzle Block, Run #35 51

LIST OF SYMBOLS

A	Nozzle Inner Surface Area, ft^2
C_p	Specific Heat of Nozzle Material, BTU/lbm °F
$C_{\alpha\beta}$	Coefficient of $T^n_{i+\alpha,j+\beta}$ in the Finite Difference Expression for $T^n_{i,j}$
C	Coefficient of $T^{n-1}_{i,j}$ in the Finite Difference Expression for $T^n_{i,j}$
E	Preset Error Limit in the Numerical Solution Procedure
g	Heat Source Term in the Heat Conduction Equation, BTU/ft^3 hr
k	Thermal Conductivity of the Nozzle Material, BTU/ft hr °F
$\bar{n}$	Normal Direction to a Nozzle Boundary Surface
$\dot{q}$	Heat Flux, BTU/ft^2 hr
r	Coordinate in the radial direction
R_1	Nozzle Throat Radius, ft
R_2	Nozzle Inner Radius at the Inlet and Exit Locations, ft
R_3	Nozzle Outer Radius, ft
R_{ref}	Nozzle Inner Radius at any Axial Location, ft
t	Time, hr
t_h	Firing Duration, sec
T	Temperature, °F
T_0	Initial Temperature, °F
$T^n_{i,j}$	Temperature at (ξ_i, η_j) at the n^{th} Time Step, °F
$\tilde{T}^n_{i,j}$	Intermediate Approximation for $T^n_{i,j}$ in the Solution Procedure, °F
V	Volume of Nozzle Block, ft^3
x	Radial Distance Measured Outward from the Inner Radius, ft
Z	Coordinate in the Axial Direction
Z_1	Axial Distance from the Nozzle Inlet to the Nozzle Throat Location, ft
Z_2	Axial Distance from the Nozzle Inlet to the Nozzle Exit Location, ft

α	Thermal Diffusivity of the Nozzle Material, ft^2/hr
δ	Radial Thickness of a Hollow Straight Cylindrical Duct, ft
η	Transformed r Coordinate in the Computational Plane
θ	Coordinate in the Azimuthal Direction
ξ	Transformed z coordinate in the Computational Plane
ρ	Density of the Nozzle Material, lbm/ft^3
ω	Relaxation Factor, a Parameter used in the Solution Procedure
ΔT	Temperature Rise, °F
$\Delta\eta$	Grid Size in the η Direction
$\Delta\xi$	Grid Size in the $\xi Direction$

Subscripts

i	Location Corresponding to $\xi = \xi_i$
j	Location Corresponding to $\eta = \eta_j$

Superscripts

n	Time Step

CHAPTER 1

INTRODUCTION

Magnetohydrodynamic(MHD) energy conversion is one of the prime technology choices for satisfying the pulse power requirements for the advanced weapon systems of the Strategic Defense Initiative(SDI). However for an MHD system to be competitive with alternative concepts, it needs to demonstrate larger characteristic power per unit weight and volume of the system, than has been done in the past.

Optimization of a particular MHD system requires the maximization of two interrelated parameters: the power density and the specific energy. The power density is the ratio of the electrical energy output to the internal volume of the generator channel. Larger power densities permit the channel, magnet, combustor, and the flow train to be smaller and lighter. The second parameter, the specific energy, is the ratio of the electrical energy output to consumable energy used for its production. For short operating durations, the power density is the dominant parameter and for long durations it is the specific energy that is dominant for minimizing the overall system weight and volume.

An experimental program to demonstrate the feasibility of high power density operation in a laboratory scale combustion driven MHD generator was conducted by the University of Tennessee Space Institute(UTSI)[1]. Losses in an MHD generator channel scale with the internal area of the device while power generated scales with the internal volume. Since volume increases faster than area for a linear MHD channel, large generators are generally more thermally efficient than their equivalent smaller versions. In a laboratory scale device

the use of a high energy fuel or a high intensity magnetic field can partially compensate for the higher losses. The experimental phase of the UTSI program was limited to using an existing moderate field strength magnet with a nominal field strength of 3.2 Tesla. The power density is proportional to the product of the square of the applied magnetic field strength and the plasma electrical conductivity. To compensate for the moderate field strength available, a highly energetic fuel, that is, one with a high heat release during combustion, was used to provide a high plasma temperature and, as a result, a high plasma electrical conductivity when appropriately seeded with an alkali metal salt.

For the present program the high energy fuel of choice was a mixture of powdered aluminum and carbon seeded with potassium carbonate and burned with gaseous oxygen. The solid fuel was burned in a hybrid combustion scheme wherein the seed bearing fuel was cast within a cylindrical combustor, and gaseous oxygen which supported the combustion, was supplied externally. The external supply of the oxygen made it possible to stop and restart the combustor. There was a lack of information, knowledge and experience in the combustion of this particular fuel-oxidizer combination and no practical precedent for its use in the hybrid combustor existed before the UTSI program.

The flow train components were designed for short duration testing using heat sinking design concepts. As part of the program cost management, it was also intended to utilize to the extent possible existing hardware, instrumentation and equipment. The experiment was designed to be compatible with an existing magnet and resulted in the combustor itself being partially within the magnet bore. This was a departure from conventional design standards which suggest that only the active portion of the generator channel be inside the magnet bore to reduce parasitic eddy currents and commensurate losses in efficiency.

The fact that the experimental flow train was largely within the magnetic field also limited the experimental instrumentation, since it is expensive to compensate for the inductive coupling of electronic sensors in the presence of a strong magnetic field . The instrumentation was limited first to the extent required for safety of operation and second to the minimum amount commensurate with the goal of experimentally demonstrating high power density. Hence, the experimental data was limited to gross channel output current and voltage, magnetic field strength, fuel and oxidizer flow rates, flow train external temperatures, a few internal temperatures and the combustor pressure. Although instantaneous oxidizer flow rates were measured, only average fuel consumption could be calculated based on changes in component weight and dimensions.

When the high energy fuel was burned in the combustor, a very high temperature plasma was generated. This plasma then passed through a series of flow train components and the whole process lasted for a very short time, typically of the order of a few seconds. The short duration of the experiments, resulted in large amounts of heat being released over a short time duration. The flow train components, designed for short duration testing using heat sinking design concepts, were in turn subjected to very high heat fluxes. This resulted in rapid temperature increases in the plasma exposed surfaces of these components and a more prolonged thermal soak out after the run. For the objectives of the test, the high surface temperatures of the components are desirable since they result in reduced power take off losses. On the other hand, the soak temperature is pertinent from the structural integrity of the component.

The flow train included a graphite nozzle, the performance of which was critical due to several reasons. Excessive temperatures could lead to erosive enlargement of the nozzle throat, which in turn could lower combustor pres-

sure, alter exit Mach number and lower the power density of the system. The nozzle surface could also lose material due to mechanical erosion by condensed aluminum oxide species resulting from combustion. Downstream of the nozzle throat is the portion where the plasma flow accelerates supersonically. The nozzle surface contour in this region should be aerodynamically smooth to avoid oblique shock formation or flow separation. The end of the nozzle mates to a generator channel. Low surface temperatures in the nozzle and boundary layer in the nozzle would similarly result in low temperature in the channel, lower plasma conductivity near the wall and hence higher voltage drop losses.

The highest temperatures in the nozzle occur on the inner surface exposed to the plasma flow at the throat. The experiments were not instrumented to measure these temperatures as the thermocouple penetrations could become vulnerable leakage spots for the hot gas. This is extremely undesirable and dangerous as well, since the nozzle operates under a high pressure. Another reason for not including these temperature measurements was the presence of the magnetic field which can introduce spurious inductively coupled signals which require conditioning. Even though these nozzle surface temperatures were not measured, they are very important from the view of the nozzle performance. Such data could give reasonable insight into the extent of possible thermochemical ablation of the nozzle inner surface and its effect on maintaining the correct dimensionality and geometry.

Pre-experiment design estimates of the transient temperature field in the nozzle were based on a one dimensional transient heat transfer model and the nozzle was designed accordingly. The heat transfer through the nozzle is inherently two dimensional; heat can be conducted both axially and radially. Initially, in accordance with the one dimensional approximation, it was assumed that the

axial heat conduction could be neglected. Even though this was a reasonable assumption, it is not quite correct and can result in the over design of the nozzle. That is, the axial conduction could be used to advantage in optimizing a design, since the one dimensional radial design may provide excess heat sinking material through its neglect of simultaneous axial conduction.

A more appropriate approach would be to use a two dimensional transient thermal analysis to design the nozzle and the generator heat sinking capacity. The objective of this study was to develop such a procedure and apply it to the interpretation of the results of this study. Such a model would be applicable to the design of generator and the fuel grain as well. However, in the present study its applicability to the nozzle only was considered as the nozzle is desired to be as short as possible and the two dimensional effects are consequently more pronounced.

The study consisted of numerically modeling the two dimensional transient heat transfer in the nozzle, with the initial and boundary conditions consistent with those that existed during experiments. It also includes a comparison of the numerical model against analytical results for some simpler degenerate geometries and boundary conditions. Validation of results of the model with data obtained during the experiments is the major effort. A successful model could predict the temperatures on the nozzle inner surface, which forms very important data for reasons already mentioned.

Chapter two describes the experimental set-up and the numerical model in detail. Chapter three compares results of the model with analytical solutions, describes available experimental data and compares the results of the modeling with the experimental data. Chapter four lists the conclusions and recommendations of this study.

CHAPTER 2

ANALYSIS

2.1 EXPERIMENTAL SET-UP

The whole experimental system consisted of the following major subsystems: combustor-nozzle, channel, exhaust duct, magnet, load bank and the oxygen, and nitrogen supply systems. Figure 2.1 shows a schematic of the set-up. This section briefly describes the various components of the experimental set-up.

A typical experiment consists of the fuel burning in the combustor, and the combustion products passing through the channel, the exhaust duct and out into the atmosphere. The oxidizer, and the purge cooling are externally supplied. The magnet, which encloses the channel and part of the combustor, is energized during a power generation run. The load bank handles the electrical energy generated in a powered generator channel test. The magnet was left deenergized during some of the tests which were intended to verify the thermal reliability of the flow train.

A magnet, with a nominal field strength of 3.2 Tesla was used in the tests. This imposed restrictions on the size of the generator channel. The channel was made cylindrical instead of rectangular even though the latter would use the available volume inside the magnet bore more effectively. This was done to avoid the high cost of rectangular channels and a corresponding complex nozzle geometry. Channels with two different configurations, continuous electrode Faraday and diagonal wall, were built for testing.

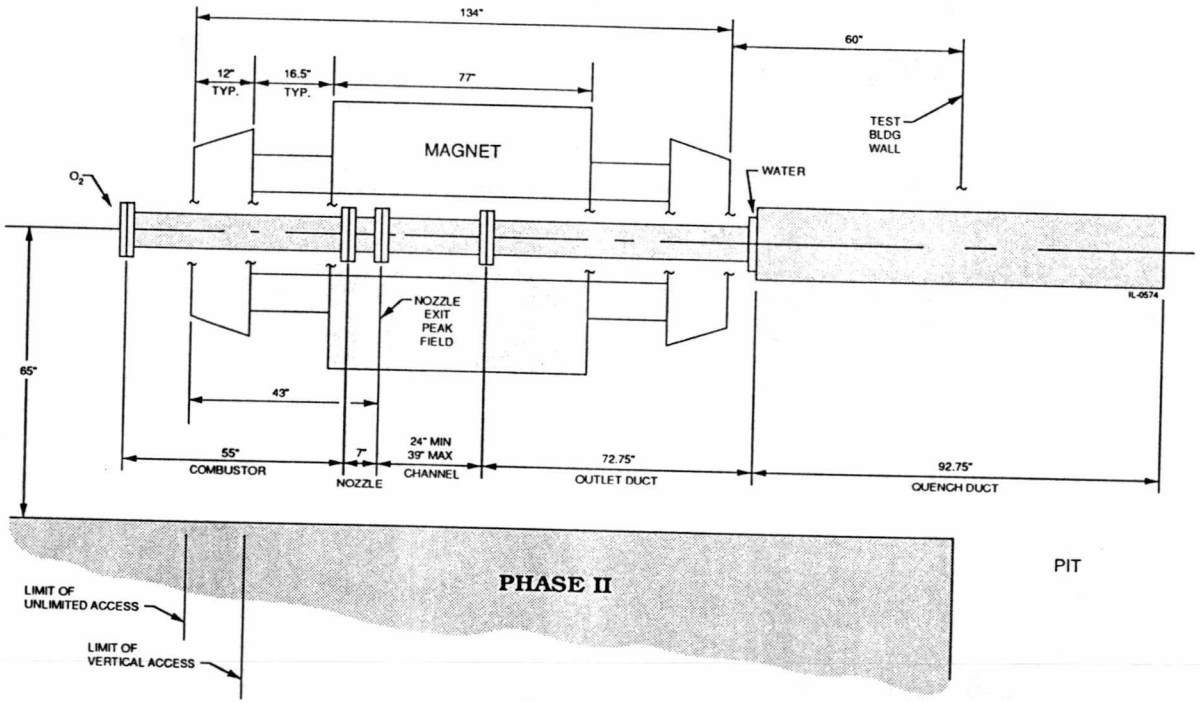


Figure 2.1 Experimental Set-up

The supply pressures for the gaseous oxygen and nitrogen that were part of the existing facility were inadequate for the requirements of the present program. A separate high pressure gaseous oxygen supply was used for the testing and was comprised of a group of bottles. The bottles were charged to 2200 psi and contained approximately 21 pounds of gas each. Ten such bottles were used to supply 1200 psi gas and maintain choked injection orifices at the design combustor pressure of 600 psi. Nitrogen purge was tied to the oxygen supply with a pneumatically operated valve. A check valve prevented back flow of oxygen, from the oxygen supply lines which were at a substantially higher pressure compared to the nitrogen supply. With the nitrogen valve open, lowering pressures in the combustor due to closure of oxygen lines automatically initiated purge by opening the check valve. Purge flow rate was approximately 1/6th the oxygen flow or approximately 0.6 lbm/sec. The purge connection was located just downstream of the last valve on the oxygen line, which in turn was located as close as possible to the combustor manifold. This was intended to reduce effective line volume upstream of the combustor, to terminate operation earlier and to enhance safety of operation. In testing, the oxygen trapped in the lines could be safely bled off after the operating sequence was over.

The nominal combustor design is shown in figure 2.2. The combustor was made of three metal pieces: the barrel, the injector face, and the nozzle. The downstream end flange was made smaller to satisfy the magnet bore dimensional constraint. The combustor was designed to operate at a nominal pressure of 600 psi with a gaseous oxygen supply at a pressure of 1200 psi.

The fuel grain had an outer diameter of six inches and was enclosed in a laminated glass shell of 1/8 inch wall thickness. This grain-shell combination was in turn separated from the stainless steel barrel by a half inch thick insulator.

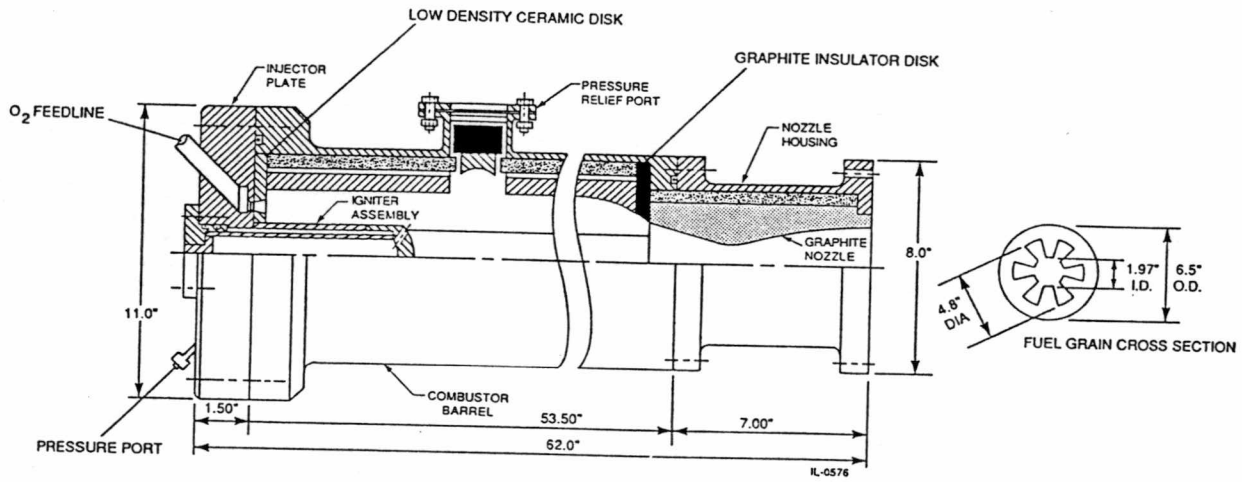


Figure 2.2 Combustor-Nozzle System

As the figure shows, the internal shape of the fuel grain resembled that of a six spoked wheel to maximize the surface burning area. This cross-section was uniform for most of its length excepting the ends. At the nozzle end, the spoke outer radius was reduced to match the nozzle contour. At the ignitor end, the grain was cylindrical and had no spokes for a length of 6.5 inches. The total internal area of the fuel grain was 9.5 ft^2.

The required fuel consumption rate mainly governs the choice of fuel grain length, while the diameter is set primarily by the magnet bore width. The density and the characteristic regression rate of this fuel were both initially unknown. The area of 9.5 ft^2 was arrived at using reasonable estimations of these unknowns. The regression rate was chosen based on experience with other aluminum based grains and the density was estimated by using suitable allowances for packing efficiency and the binder. The reducing environment created by a sub-stoichiometric combustion was advantageous as graphite was used as the main internal thermal shield.

A pressure relief port, located approximately midway along the length of the combustor, was provided in the combustor barrel as shown in figure 2.2. This relief port was to be positioned vertically between the coil force containment structures, when installed in the magnet. The relief port was meant to provide an open port to the combustor main cavity in the case of excess pressure.

The front end flange of the combustor was a blind flange with a central opening to house the ignitor assembly. Within the combustor side end of this flange was also located an oxygen manifold, which lead to six injector holes. These holes were positioned in such a way that oxygen is injected along the fuel grain cavities between the spokes. In accordance with the heat sinking design,

the fuel grain is thermally insulated from the outer steel pressure vessel.

The ignitor consisted of a stainless steel body, a fuel lined barrel and a nozzle with six orifices. The barrel contained a central perforated stainless steel tube, loaded with a group of pellets comprised of a mixture of boron and potassium nitrate. An electric match, with leads located outside the combustor, ignited the pellets when fired. This in turn fired the fuel inside the barrel and the combustion products exited through the six orifices into the interspoke fuel grain cavities. The presence of oxygen ignited the fuel grain. While the pellets burnt in milliseconds, it was the main fuel charge in the barrel that provided hot flame for the combustor main fuel grain for approximately two seconds.

The downstream end of the combustor houses the nozzle assembly. This consisted of a graphite nozzle surrounded by a ceramic insulator and encased in a double flanged stainless steel shell. The nozzle was replaceable as it was expected to erode significantly. It is pertinent to note that the graphite nozzle itself was similar to the fuel grain. That is, the nozzle could be thought of as a solid fuel as well. The fuel grain was a relatively loose or low density compaction of carbon and aluminum particles with a binder designed for relative ease of thermal decomposition. On the other hand, the nozzle was a high density granular structure intended to inhibit its thermal decomposition. It was the relative differences in density as well as the preferential burning of the fuel grain that was key in preventing the nozzle from being consumed as well. In addition, the condensed aluminum oxide species may mechanically erode the graphite in the nozzle through grazing impact. The nozzle was designed to expand flow from combustor conditions to an exit Mach number of 2.5. The area ratio of 4.0 required for this expansion, along with a specified exit diameter of 3.0 inches, the throat diameter had to be 1.5 inches.

The plasma flow accelerated supersonically downstream of the nozzle throat. This region was contoured aerodynamically to avoid oblique shocks and flow separation. The nozzle exit also transitioned smoothly into the generator entrance without any misaligned steps or angular discontinuities. The nozzle design is shown in figure 2.2. The nozzle was 8.0 inches in overall length with the subsonic portion upstream of the throat being 3.0 inches long. The 5.0 inch long supersonic region was contoured in accordance with inviscid method of characteristic calculations.

As part of the instrumentation, the combustor had a pressure port and three thermocouples in the nozzle. The three nozzle thermocouples were located on the outer surface of the nozzle block but inside the steel shell and insulating refractory. Axially these thermocouples were located one inch after the inlet, directly in line with the throat, and one inch before the exit. The internal instrumentation was kept to a minimum to avoid potential plasma leaks through shell penetrations.

The whole set-up could be tested by either mounting it on the facility floor or by mounting it on a test stand. Floor mounting was used for the first four of the seven combustor firings; the test stand had to be used for the remaining runs to locate the flow train inside the magnet.

2.2 NUMERICAL MODELING

2.2.1 PROBLEM FORMULATION

The heat conduction in the nozzle, as mentioned earlier, can be reasonably approximated as two dimensional: heat is conducted in both the radial and axial directions where large gradients are anticipated, whereas, circumferential conduction can be neglected based upon the assumption of uniform circumferential conduction and homogeneity. As the fuel was burned, the combustion products flowed through the nozzle and further down the flow train. During an experiment, the heat flux was higher around the throat region than at either end. This heat flux existed over the duration of firing, after which purge cooling through a nitrogen flow was initiated. As part of the whole experimental system, a layer of insulation covered the nozzle on its outer side. Low thermal conductivity insulation materials were on both ends of the nozzle, in the axial direction.

This section describes the steps involved in solving this heat transfer problem. Discussion of the problem in the general case is given, relevant assumptions and simplifications are stated, and the details of the numerical scheme are summarized.

The general heat conduction equation in cylindrical co-ordinate system (r,θ,z) is:

$$\frac{1}{r}\frac{\partial}{\partial r}(kr\frac{\partial T}{\partial r}) + \frac{1}{r^2}\frac{\partial}{\partial \theta}(k\frac{\partial T}{\partial \theta}) + \frac{\partial}{\partial z}(k\frac{\partial T}{\partial z}) + g = \rho C_p \frac{\partial T}{\partial t} \qquad (2.1)$$

where k is the thermal conductivity, C_p the specific heat and ρ the density- all three of the nozzle material. The term g represents a source term for the amount

of heat generated per unit volume in unit time.

The shape of the nozzle is axisymmetric. A schematic of a typical cross section along the axis of the nozzle is given in Figure 2.3. Due to symmetry, thermal gradients in the azimuthal(θ) direction can be neglected. The governing heat conduction equation that needs to be solved subject to this system is reduced by retaining only those terms containing gradients in the axial (z) and radial (r) direction and the time dependence. It is also assumed that the variation of material properties including the thermal conductivity and the specific heat with temperature is negligible. This assumption is reasonable for this study, as graphite, the material of which the nozzle is made of, does not show significant changes in these properties in the temperature ranges concerned. This fact allows the thermal conductivity, k, to be taken outside the derivatives. Also, as there are no heat sources in this problem, g is zero. Hence, for the present analysis the general equation simplifies to:

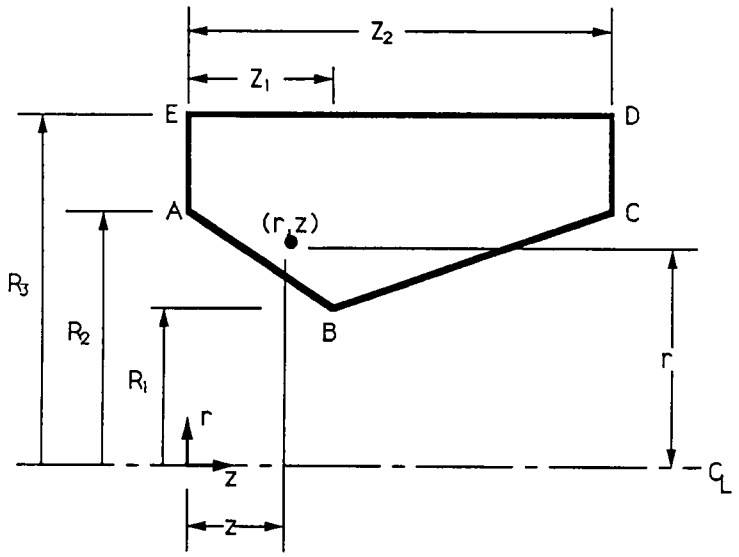
$$\frac{1}{r}\frac{\partial}{\partial r}(r\frac{\partial T}{\partial r}) + \frac{\partial^2 T}{\partial z^2} = \frac{1}{\alpha}\frac{\partial T}{\partial t} \tag{2.2}$$

where the thermal diffusivity, α is given by

$$\alpha = \frac{k}{\rho C_p} \tag{2.3}$$

It is also appropriate to point out that the temperature dependence of the thermal diffusivity of the nozzle material is less pronounced than that of either the thermal conductivity or the specific heat.

To solve the above equation a set of boundary and initial conditions are required. Along the outer and end boundaries, an adiabatic wall boundary condition is used, that is, no heat transfer across these surfaces can occur, and



R_1 = 0.75 in = 0.625 ft

R_2 =1.50 in = 0.125 ft

R_3 = 2.25 in. = 0.1875 ft

Z_1 = 2.8 in = 0.2333 ft

Z_2 = 7.8 in =0.650 ft

Figure 2.3 Schematic of Idealized Nozzle Geometry

the temperature gradients in the directions normal to these surfaces vanish. Mathematically these conditions can be stated as:

$$\frac{\partial T}{\partial \bar{n}} = 0@(r, z = 0, t)(faceEA, figure2.3) \tag{2.4}$$

$$\frac{\partial T}{\partial \bar{n}} = 0@(r, z = Z_2, t)(faceDC, figure2.3) \tag{2.5}$$

$$\frac{\partial T}{\partial \bar{n}} = 0@(r = R_3, z, t)(faceED, figure2.3) \tag{2.6}$$

where $\bar{n}$ is in the normal direction to the appropriate surface.

In the real case, there is some heat transfer from the nozzle through the insulating layer, to the outer shell which is eventually lost to the ambient atmosphere by natural convection. Similarly an unknown amount of heat is transferred through the two end faces in the axial direction. Although it is known that heat was lost this way, it is reasonable to assume that the quantity or rate of surface heat loss is negligible. Moreover the heat loss is markedly higher only after a long time after combustion is over. This study concerns the transience immediately following the firing period during which the surface heat loss is very negligible. Hence, the adiabatic surface condition used is justifiable as a reasonable boundary condition to the ideal system under analysis.

Along the inner wall, the heat transfer rate is taken to be specified as a function of the axial position during the heating period of a test. This rate is given by the form:

$$-k\frac{\partial T}{\partial \bar{n}} = \dot{q}(z)@(r = R_{ref}, z, t \leq t_h)(faceABC, figure2.3) \qquad (2.7)$$

After cessation of firing, the heat input is taken to be zero along the inside surface. That is, an adiabatic wall boundary condition is imposed following the termination of firing and is given by:

$$\frac{\partial T}{\partial \bar{n}} = 0@(r = R_{ref}, z, t \geq t_h)(faceABC, figure2.3) \qquad (2.8)$$

In equations 2.4 through 2.8, $\bar{n}$ represents the direction normal to the surface under question; t_h stands for the initial heating time during which heat is input to the nozzle. In equation 2.7, $\dot{q}(z)$ is the heat flux variation along the length. A typical heat flux distribution was chosen for each calculation, consistent with the corresponding experiment.

The equation 2.2 along with the boundary conditions 2.4 through 2.8 is the statement of the problem. The key approach to solving this problem is through a transformation of the physical (r,z) plane to a computational (ξ,η) plane. Through this transformation, the five sided nozzle shape of Figure 2.3 in the physical plane can be cast into a rectangular computational plane. The region ABC of Figure 2.3 collapses into a straight line on transformation. The transformation is illustrated in the figure 2.4. This figure also shows the mesh chosen for computations, in both the planes.

The transformations of the equations and the boundary conditions from the physical plane to the computational plane is done according to standard mathematical procedures [2]. The functions describing the transformation from

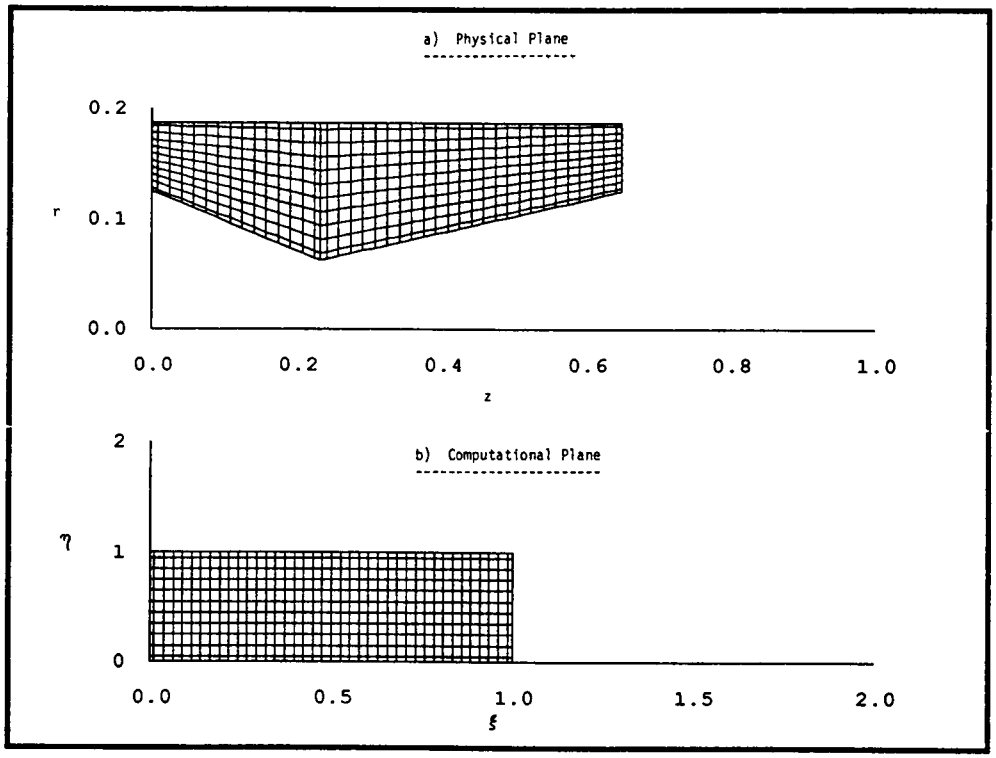


Figure 2.4 Numerical Grid in the Physical and Computational Planes

the physical plane to the computational plane, in the general case, can be represented by

$$\xi = \xi(r, z)$$

$$\eta = \eta(r, z) \tag{2.9}$$

The transformation of the partial derivatives of the dependent variable T from the (r,z) system to the (ξ,η) system is accomplished by a chain rule as given below:

$$\frac{\partial T}{\partial r} = \frac{\partial \xi}{\partial r}\frac{\partial T}{\partial \xi} + \frac{\partial \eta}{\partial r}\frac{\partial T}{\partial \eta} \tag{2.10}$$

$$\frac{\partial T}{\partial z} = \frac{\partial \xi}{\partial z}\frac{\partial T}{\partial \xi} + \frac{\partial \eta}{\partial z}\frac{\partial T}{\partial \eta} \tag{2.11}$$

Higher derivatives can be obtained by repeated applications of the chain rule. Appendix A gives a compilation of the derivatives in the computational plane.

The transformation functions used for the nozzle problem are:

$$\xi = \frac{z}{Z_2} \tag{2.12}$$

$$\eta = \frac{r - R_{ref}}{R_3 - R_{ref}} \tag{2.13}$$

where

$$R_{ref} = R_2 - \frac{z}{Z_1}(R_2 - R_1) \text{ when } z \leq Z_1$$

$$R_{ref} = R_2 - \frac{Z_2 - z}{Z_2 - Z_1}(R_2 - R_1) \text{ when } Z_1 \leq z \leq Z_2 \tag{2.14}$$

Hence, η (r,z) is a simple scaling , where the radial thickness at any axial location is used as a normalizing reference.

After applying the transformation, the governing equation 2.3 is given in the form:

$$A\frac{\partial T}{\partial \eta} + B\frac{\partial^2 T}{\partial \eta^2} + C\frac{\partial^2 T}{\partial \xi^2} + D\frac{\partial^2 T}{\partial \xi \partial \eta} = \frac{1}{\alpha}\frac{\partial T}{\partial t} \tag{2.15}$$

where the coefficients are defined as follows:

$$A = \frac{1}{r}\frac{\partial \eta}{\partial r} + \frac{\partial^2 \eta}{\partial z^2}$$

$$B = (\frac{\partial \eta}{\partial r})^2 + (\frac{\partial \eta}{\partial z})^2$$

$$C = (\frac{\partial \xi}{\partial z})^2$$

$$D = 2\frac{\partial \eta}{\partial z}\frac{\partial \xi}{\partial z}$$

2.2.2 FINITE DIFFERENCES

The finite difference forms used to approximate the partial derivatives in equation 2.15 at different points in the grid are given in Appendix B. In these equations $T^n_{i,j}$ represents the temperature T, at the grid point which is at the intersection of the vertical ξ_i line and the horizontal η_j line, at the n^{th} time step. The final result sought from the numerical solution procedure is the set of temperatures at a finite number of grid points in the rectangular grid shown in figure 2.4. These solutions are obtained at different successive time steps until a desired point of time.

2.2.3 BOUNDARY CONDITIONS

It can be seen from equations 2.4 through 2.8 that the boundary conditions for the problem are given in terms of derivatives in a direction normal to the boundary surfaces in the physical plane. It is essential that these boundary conditions also be transformed so that they can be applied for numerical calculations on the computational plane.

Let the general boundary condition be represented as:

$$\frac{\partial T}{\partial \bar{n}} = Q \tag{2.16}$$

Transforming this boundary condition to the computational plane,

$$\frac{\partial T}{\partial \bar{n}} = \frac{\partial r}{\partial \bar{n}}\frac{\partial T}{\partial r} + \frac{\partial z}{\partial \bar{n}}\frac{\partial T}{\partial z} = Q \tag{2.17}$$

assuming $\bar{n} = \bar{n}(r, z)$. Using equations (2.10) and (2.11) this could be expanded as:

$$\frac{\partial r}{\partial \bar{n}}[\frac{\partial \eta}{\partial r}\frac{\partial T}{\partial \eta}+\frac{\partial \xi}{\partial r}\frac{\partial T}{\partial \xi}]+\frac{\partial z}{\partial \bar{n}}[\frac{\partial \eta}{\partial z}\frac{\partial T}{\partial \eta}+\frac{\partial \xi}{\partial z}\frac{\partial T}{\partial \xi}]=Q \tag{2.18}$$

Rearranging terms in equation (2.18),

$$[\frac{\partial r}{\partial \bar{n}}\frac{\partial \eta}{\partial r}+\frac{\partial z}{\partial \bar{n}}\frac{\partial \eta}{\partial z}]\frac{\partial T}{\partial \eta}+[\frac{\partial r}{\partial \bar{n}}\frac{\partial \xi}{\partial r}+\frac{\partial z}{\partial \bar{n}}\frac{\partial \xi}{\partial z}]\frac{\partial T}{\partial \xi}=Q \tag{2.19}$$

That is,

$$G_1\frac{\partial T}{\partial \eta}+G_2\frac{\partial T}{\partial \xi}=Q \tag{2.20}$$

where

$$G_1=\frac{\partial r}{\partial \bar{n}}\frac{\partial \eta}{\partial r}+\frac{\partial z}{\partial \bar{n}}\frac{\partial \eta}{\partial z} \tag{2.21}$$

$$G_2=\frac{\partial r}{\partial \bar{n}}\frac{\partial \xi}{\partial r}+\frac{\partial z}{\partial \bar{n}}\frac{\partial \xi}{\partial z} \tag{2.22}$$

Using the specific values of Q from equations 2.4 through 2.8, for different boundary points in the grid, finite difference forms of the boundary conditions can be obtained. The finite difference forms of the boundary conditions for different representative points on the boundary is given in Appendix C.

2.2.4 FINITE DIFFERENCE EQUATIONS

For an interior point (i,j) in the rectangular computational plane, using the finite difference forms of derivatives given in Appendix B, a resulting finite

difference equation can be obtained for $T^n_{i,j}$. The equation for such an interior node is of the form

$$\tilde{T}^n_{i,j} = (\sum_{\alpha,\beta=-1}^{1} C_{\alpha\beta} T^n_{i+\alpha,j+\beta}) + C^* T^{n-1}_{i,j} \tag{2.23}$$

where $\tilde{T}^n_{i,j}$ is a new approximation for $T^n_{i,j}$ using values of temperatures at neighboring points given on the right hand side of equation 2.23. Such equations can be obtained for points on the boundary as well. The only difference being that the finite difference approximations of boundary conditions given in Appendix C are also to be considered in deriving these equations. Equations for boundary points are typically of the form:

$$\tilde{T}^n_{i,j} = (\sum_{\alpha,\beta=-2}^{2} C_{\alpha\beta} T^n_{i+\alpha,j+\beta}) + C^* T^{n-1}_{i,j} \tag{2.24}$$

2.2.5 SOLUTION PROCEDURE

The procedure used to solve for temperatures at grid points for a particular time step, using the values at the previous time step, is iterative in nature. This results from the fact that the expressions for the new approximations, contain temperatures of some other grid points at the current time step which are essentially unknown. Hence it is aimed to successively refine the approximations until the difference between two successive approximations is within a predetermined limit, for all the points in the entire grid system.

This method of solution is achieved by a point-to-point successive under relaxation procedure as given below,

$$T^n_{i,j}|_{new} = T^n_{i,j}|_{old} + \omega(\tilde{T}^n_{i,j} - T^n_{i,j}|_{old}) \tag{2.25}$$

where ω = relaxation factor, a constant.

The relaxation factor used for the computations in this study was typically 0.9. These calculations are carried out for the entire grid by moving from one point to the next. The approximations at points along one ξ_i are computed first, to enhance faster diffusion of boundary information into the grid. For this reason, the computations begin from points closest to the nozzle inner face and proceed towards the nozzle back face. This is done, since the dominant boundary condition is on the nozzle inner face, ABC of Figure 2.3, where heat is input to the nozzle. The iterations for a particular time step are stopped when the condition that

$$\frac{T^n_{i,j}|_{new} - T^n_{i,j}|_{old}}{T^n_{i,j}|_{new}} \leq E \tag{2.26}$$

is satisfied for all the grid points. 'E' is the preset error limit, the typical value used being 0.001. Once this condition is satisfied for all the grid points, the array $T^{n+1}_{i,j}$ is updated by values in the array $T^n_{i,j}|_{new}$ as given below

$$T^{n+1}_{i,j} = T^n_{i,j}|_{new} \quad \forall i,j \tag{2.27}$$

The whole set of iterative calculations is repeated for successive time steps until the desired point of time. This scheme gives the temperature field in the entire grid system at different times.

CHAPTER 3

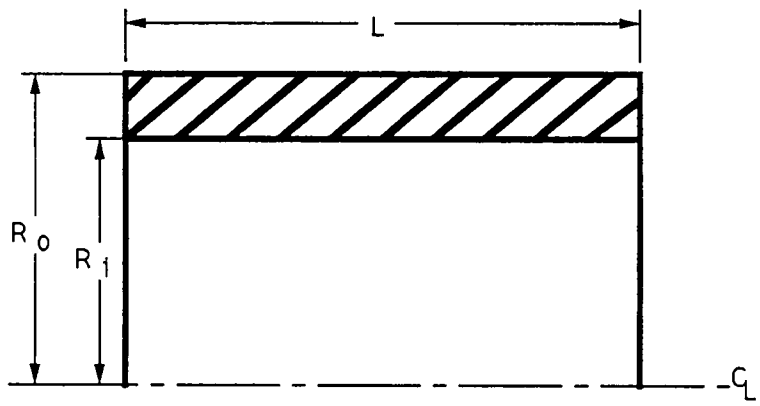
RESULTS

3.1 COMPARISON OF NUMERICAL AND ANALYTICAL SOLUTIONS

It is general practice to verify the performance of a numerical model by comparing its results against known solutions when possible. The numerical scheme outlined in chapter two was applied to a simple problem for which the solution already existed in the literature. This was done for a simple problem: the transient heat transfer in a thin, long straight cylindrical shell. That is, the two dimensional solution procedure is applied to a one dimensional problem having a known solution. This section reviews this work.

The problem selected was the case of a long, hollow, straight cylindrical duct subjected to uniform heat flux along the length on the inner surface for a fixed time, after which it is allowed to equilibrate. The other surfaces of this body are insulated. Referring to figure 3.1, the ratio of thickness to the mean radius of the duct was chosen to be 0.1. This was done as the results were to be compared with the case of a slab heated on one face and insulated on the other face. To make this problem represent the heated slab, the ratio mentioned above had to be much smaller than unity.

The transient heat transfer in the slab, for which the analytical solution was obtained from Reference 3, is one dimensional. The geometry, dimensions etc., for the numerical case were also chosen such that the heat transfer would be as close to being one dimensional as possible. Relevant details are shown in



Mean Radius, $R_m = \frac{R_i + R_o}{2}$

Thickness, $\delta = R_o - R_i$

$\frac{\delta}{R_m} = 0.1$

$x = r - R_i$

Figure 3.1 Geometry and Problem in the Case of a Straight Cylindrical Duct

figure 3.1.

The results of these calculations are given in the figure 3.2. This figure shows the variation of temperature with time at different radial locations as computed numerically and analytically. Figure 3.2 a) is for the initial heating period and figure 3.2 b) is for the equilibrating duration, during thermal soak after the cessation of heat input occurred. The results are plotted in terms of dimensionless parameters. It can be noted that the results of the numerical model match quite favorably with the analytical solution.

3.2 EXPERIMENTS AND DATA

This section describes in detail, the experiments and the relevant data obtained from these tests.

3.2.1 EXPERIMENTS

As part of the UTSI SDI program, a series of test runs were conducted on the combustor and the MHD generator system. The construction details of components, relevant to this study are given first. Experimental aspects and the data are discussed next.

The program warranted a highly energetic fuel so that safe high power density operations could be demonstrated. For this program, the high energy fuel of choice was a mixture of powdered aluminum and carbon seeded potassium carbonate and burned with gaseous oxygen. The solid fuel was burned in a hybrid combustion scheme wherein the fuel was cast within a cylindrical combustor in analogy with a solid propellant rocket motor.

The hybrid combustor comprised of a fuel grain cast within the

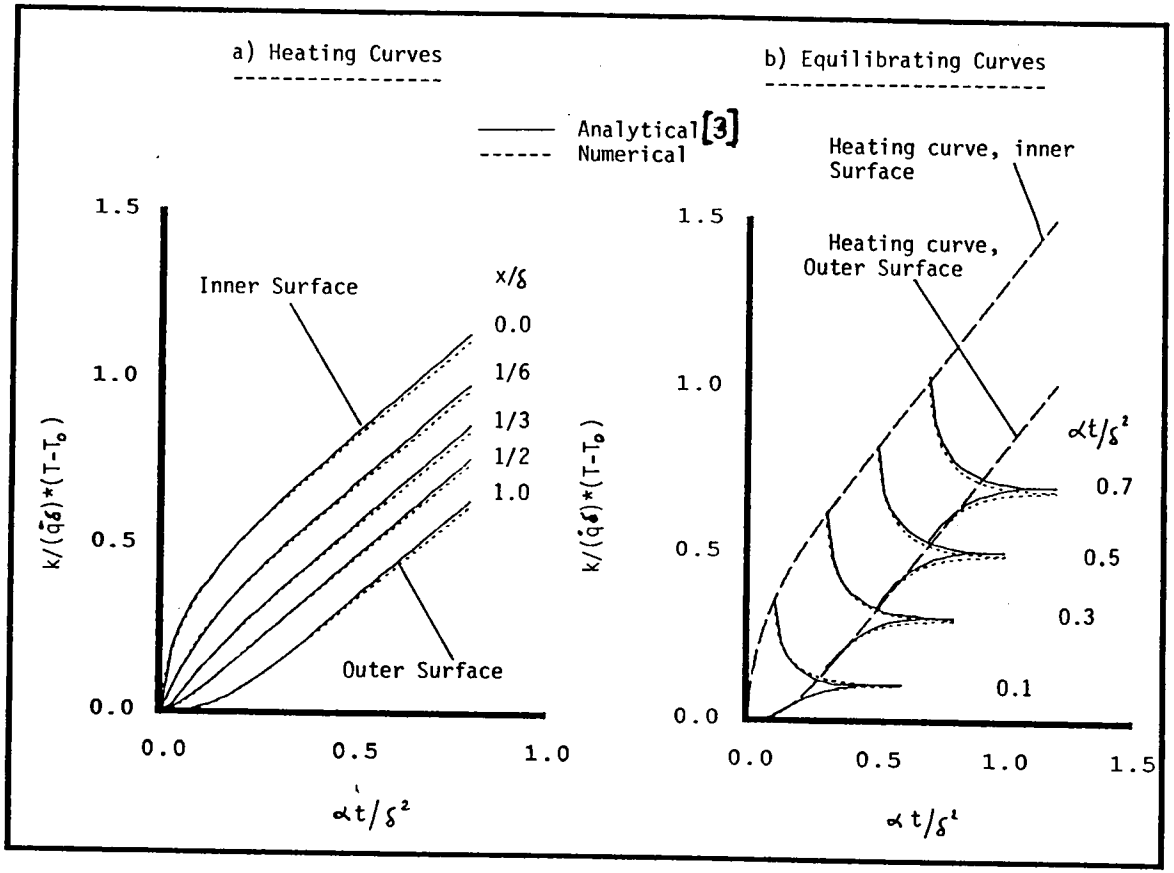


Figure 3.2 Comparison of Numerical and Analytical Solutions[3], Straight Cylindrical Duct, Uniform and Constant Heat Flux: a) Heating Curves, b) Equilibrating Curves

combustor with the gaseous oxygen oxidizer supplied externally to the combustor. The nozzle had an outer structural shell and interchangeable, variable internal graphite inserts for multiple testing and variable operation. There was also a layer of insulation between the nozzle housing and the actual graphite nozzle. A complete description was given in section 2.1 and can be returned to for references.

During the course of the program, the various components and systems were tested separately and in combination. The tests were performed to verify safe operation, expected performance, repeatability and adequacy of the instrumentation. This section describes tests conducted on the combustor system.

Seven firings of the combustor using five fuel loads, with a cumulative run time of 13.9 seconds, were performed during the program. The first three firings were with the combustor and exhaust ducts mounted on the facility floor. The fourth firing was performed on a test stand mounted between the open magnet halves. The last three firings were with the magnet closed about the flow train and energized. All facility testing was identified by a sequential numbering system which included oxidizer system check out initially and prior to each run. As a consequence, the resulting firing tests bear sequential but nonuniformly increasing numerical designations.

The initial firing, designated Run #7, was a planned 3-second test but automatically terminated at 1.38 seconds into the run when the inner face of the oxygen manifold burned up. This in turn, allowed the oxygen feed line to dump into the combustor, resulting in an over pressure which was sensed and precipitated the shutdown.

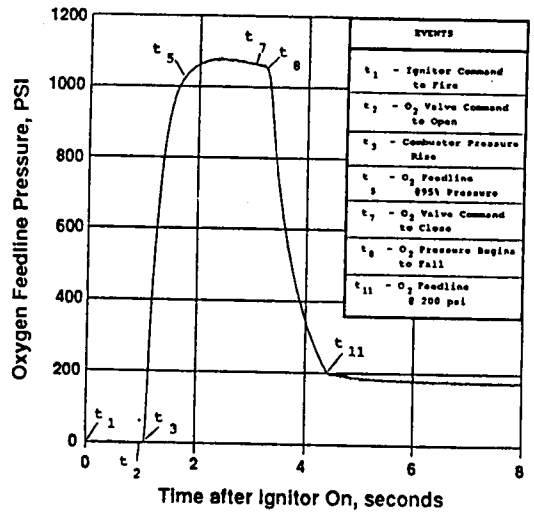
The second combustor firing, Run #10,went full duration with no observed leakage of hot gas to the exterior of the ignitor or the nozzle thermocou-

ple lead penetration. The third combustor firing, Run #20, used the same fuel grain and went through a planned run duration of 1.5 seconds. It was mainly intended to verify a new ignitor design. From previous tests, it was clear that the exposed ignitor components were being consumed and they required thermal protection.

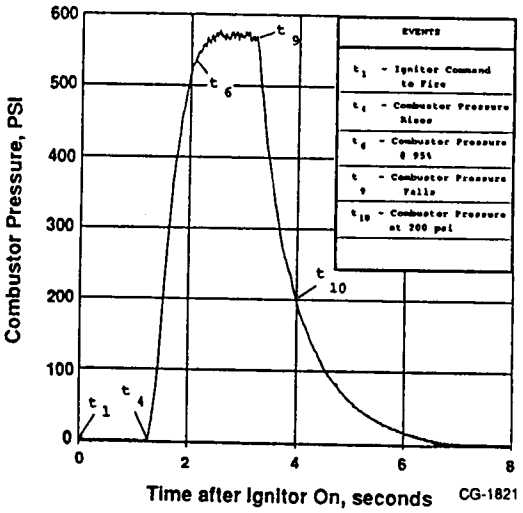
The fourth combustor firing, Run #24, used a fresh fuel grain. Silicone rubber gaskets were installed on either side of the graphite disc to prevent back flow between the outer surface of the fuel grain and inner combustor wall. The fifth test, Run #28, also used a fresh fuel grain and was conducted to measure Faraday channel power. Nozzle erosion was very minimal. The sixth test, Run #32, lasted its intended firing duration of 1.5 seconds. The seventh and final test of the program, Run #35, was an extended duration repetition of Run #32. A fresh fuel load was used and the firing duration was 4.0 seconds. This was the longest firing duration for all the tests in this program. The firing went its intended duration with no hardware problems encountered. As a consequence of the extended duration, temperatures recorded on the flow train were generally higher than observed before but all within tolerable bounds.

3.2.2 COMBUSTION TEST DATA

Instrumentation on the combustor was sparse. It included combustor pressure, oxygen feeding pressures, and external thermocouples. In addition, the oxygen bottles and fuel grains used during the tests were weighed to determine their mass loss and infer flow rates to evaluate the combustion characteristics. Figures 3.3a and 3.3b show examples of pressure data. In these figures, various event times can be used as means for comparison of the combustor performance. Such a compilation is given in tables 3.1 and 3.2. The events are largely



a) Oxygen Feedline Pressure



b) Combustor Pressure

Figure 3.3 Typical Combustor Pressure Data Showing Event Times

TABLE 3.1

Combustor Test Summary: Event Chronology

Time	Event	Time in Seconds						
		7	10	20	24	28	32	35
t_1	Igniter command to fire	0	0	0	0	0	0	0
t_2	O_2 valve command to open	1.00	1.00	1.00	1.00	1.00	1.00	1.00
t_3	O_2 line pressure rises	1.11	1.17	1.06	1.10	1.10	1.08	1.08
t_4	Combustor pressure rises	1.26	1.29	1.10	1.14	1.18	1.14	1.14
t_5	O_2 line @ 95% pressure	1.95	2.00	1.71	2.00	1.90	1.92	1.92
t_6	Combustor @ 95% pressure	1.98	2.12	2.08	2.15	⋆	2.12	2.14
t_7	O_2 valve command to close	2.38	3.00	3.00	2.50	2.50	2.50	5.00
t_8	O_2 line pressure falls	2.38	3.14	3.22	3.18	2.61	2.69	5.10
t_9	Combustor pressure falls	2.55	3.22	3.30	⋆	⋆	2.69	5.22
t_{10}	Combustor pressure @ 200 psi	⋆	4.00	4.00	⋆	⋆	3.16	6.24
t_{11}	O_2 line pressure @ 200 psi	3.35	4.43	4.41	3.67	3.18	3.18	5.67

⋆ Data Lost

TABLE 3.2

Combustor Test Summary: Measured and Derived Parameters

Parameters	Run No.						
	7	10	20	24	28	32	35
Test Time, $(t_9 - t_6)$ sec	0.57	1.10	1.22	1.15#	0.57#	0.57	3.08
Run Time, sec	2.23	2.76	2.88	2.81	2.23	2.23	4.74
Thermal Time, $\frac{1}{2}(t_{10} + t_9 - t_6 - t_4)$, sec	1.65	1.90	2.06	2.00#	⋆	1.29	4.09
Peak Combustion pressure, psi	633	570	500	537	⋆	629	617
Peak O_2 line pressure, psi	1274	1171	1077	1111	1126	1135	1135
Oxygen flow rate, kg/sec	1.71	1.57	1.34	1.50	1.58	1.54	1.53
Fuel weight loss, kg	4.20	5.00	3.98	4.34	6.36	5.51	9.51
Fuel flow rate, kg/sec	1.88	1.81	1.38	1.54	2.85	2.47	2.00
Oxygen/Fuel ratio	0.91	0.87	0.96	0.97	0.55	0.62	0.76
Fuel recession rate, cm/sec	0.133	0.128	0.098	0.109	0.202	0.175	0.142
Mass Flow, kg/sec	3.59	3.38	2.72	3.04	4.43	4.01	3.53

⋆ Data Lost # Estimated

self explanatory with the exception of a few comments. Events 1,2, and 5 are preset computer controlled events. All times are referenced to the time at which the ignitor command to fire was initiated by the computer controller.

The combustor transient characteristics are readily discernible from the data. For example, there are relatively consistent delays in opening and closing the oxygen valve, rise time in the combustion pressure, etc. Of particular importance to this study is the thermal exposure time. Components are subjected to heating during the combustor rise and fall as well. A thermal exposure time has been defined as the interval between the midpoints of ramp up and ramp down of combustor pressure and is comparable with the average run time. This is given in table 3.2. Note that in keeping within the constraints of the heat sinking design all runs were of very short duration. The thermal exposure times varied from 1.29 seconds to 4.09 seconds with six of the seven cases having thermal times less than 2.0 seconds.

In the nozzle assembly, three internal thermocouples were installed on the back or outside face of the nozzle graphite block. These thermocouples were axially located one inch cm from the entrance, at the throat location and one inch from the exit. Due to difficulty of providing lead outs through the pressure vessel, these were the only thermocouples mounted interior to the flow train components. By referring to figure 3.4, these thermocouples were installed between the graphite and its outer ceramic insulator within the steel nozzle shell. The thermal response of the thermocouples for a typical run is given in figure 3.4. An unexpected behavior occurs in that in certain instances an immediate temperature rise at the onset of combustion is evident as indicated in the figure. Also, a longer than anticipated period after combustion results where the temperature continues to increase. It is believed that the

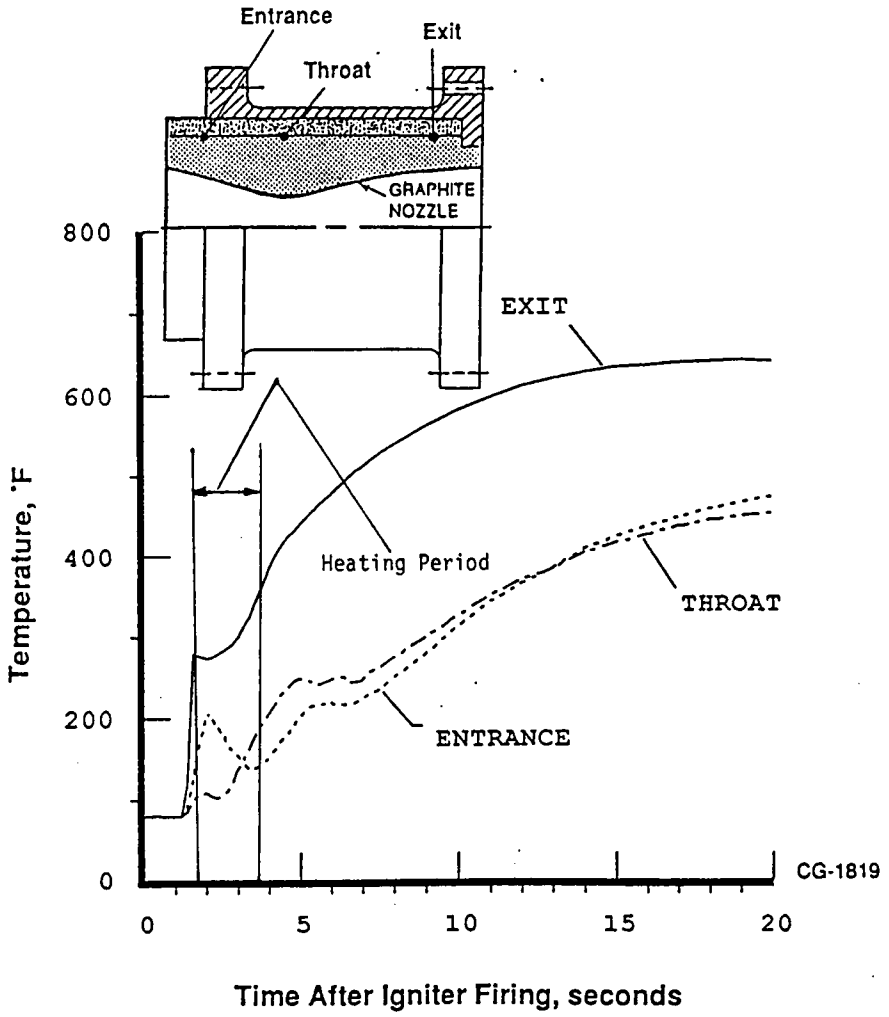


Figure 3.4 Typical Nozzle Temperature Transients Following a Firing (Test Run #10)

initial temperature rise response may be due to combustion gas leakage through the porous insulator along the thermocouple lead out wire grooves and occurs during initial pressurization as the combustor fires. The long temperature rise time after firing is the characteristic thermal soak of the nozzle.

At the end of the combustion, nitrogen is introduced to primarily quench the fuel grain but it also provides some cooling to the flow train. The nitrogen flow rate is around one sixth the oxygen flow. Thus for a short period of time following firing, the purge cooling is ineffectual. That is, the heat pulse will diffuse through the graphite faster than it can be removed at the inner surface by convection to the nitrogen purge. This fact is evident in the data and appears to be the case for the first twenty seconds following termination of combustion.

3.3 COMPARISON OF NUMERICAL RESULTS AND EXPERIMENTAL DATA

3.3.1 THE COMPARISON

As explained previously in section 2.2, experiments have been conducted on the combustor-nozzle system. Efforts have been made to simulate these conditions numerically and compare the results with the experimental data. The rest of this section describes the numerical simulation and how the results compared with the experimental data.

From the experimental data, it was evident that the heat flux was higher in the vicinity of the throat than at the ends. This is also reasonable from the physics of the particular flow as well. A higher Reynold's number and hence a higher heat transfer coefficient should be expected at the throat region compared to the ends. This conclusion can also be arrived at based on the

following arguments.

Using properties of the nozzle material at mean experimental temperatures, a thermal diffusivity was calculated. With this, a one dimensional calculation was performed for each of the three cross-sections at the thermocouple locations. It should be noted that the thickness of nozzle material separating the heat flux surface and the thermocouple is, at the throat, twice as much as it is at either ends. In one dimensional heat conduction, the temperature rise at a point over a fixed time varies directly as the thermal diffusivity of the material, and the heat flux and inversely as the distance separating the point from the heat input location. Hence, as expected, the one dimensional calculations showed that significantly higher temperatures would be noticed at the ends, than at the throat, when subjected to the same heat flux. This prompted the deduction that higher heat fluxes must have existed around the throat. It was also clear from experimental data, where all the three thermocouples mounted on the nozzle back face showed about the same rate of temperature rise.

Based on the above analysis, an axial heat flux distribution was chosen for each calculation such that $\dot{q}_i A_i / V_i$ was constant for all i, where each i stands for a particular cross section perpendicular to the nozzle axis. The resulting heat flux distribution, has a higher heat flux in the vicinity of the throat, compared to the ends. Care was also taken to satisfy energy conservation, that is,

$$t_h \sum_i \dot{q}_i A_i = \rho C_p (\Delta T) V$$

corresponding to that experiment. Here, t_h is the thermal exposure time, $\dot{q}_i$ and A_i are the heat flux and inside surface area at the axial location i respectively, V is the total nozzle block volume and ρ and C_p are the density and specific

heat of the graphite respectively. An example of such a distribution chosen for one particular calculation, run #35, is shown in figure 3.5.

Here 'ΔT' stands for the temperature rise of the nozzle in an ideal equilibrating situation, that is, under conditions similar to those assumed for the calculations. This requires that the nozzle outer and end boundaries be insulated during the heating period and all the boundaries be insulated thereafter. As this was not true of the actual experiments, the following procedure was adopted to deduce the temperature rise for each experiment.

The temperature rise, 'ΔT', was estimated as the difference between the maximum recorded temperature among the three nozzle thermocouples, and the initial temperature recorded at the start of the experiment. Figure 3.6 gives the thermocouple response for run #35 over a period of 1000 seconds after ignition. It can be noticed that a maximum temperature of 780 degrees F was recorded by the thermocouple at the nozzle entrance location. The initial temperature, though not shown in this figure, was 58 degrees F for this experiment. Hence, for this calculation, the ΔT was reasonably assumed as 720 degrees F ($\approx 720 - 58$ degrees F). A similar procedure was adopted for other calculations as well.

The numerical calculation was performed for six of the seven experiments, that is all the experiments excepting run #7, which was the initial run during which the thermocouples were lost. The thermocouple responses from this test were similar in character to the data from some of the other tests discussed later. This fact prompted us to believe that the strange kinks in these data were most possibly due to hot gas leaks. The gas leaks and the consequent damage of thermocouples in run #7 also further the point that the thermocouple lead outs are a problem source.

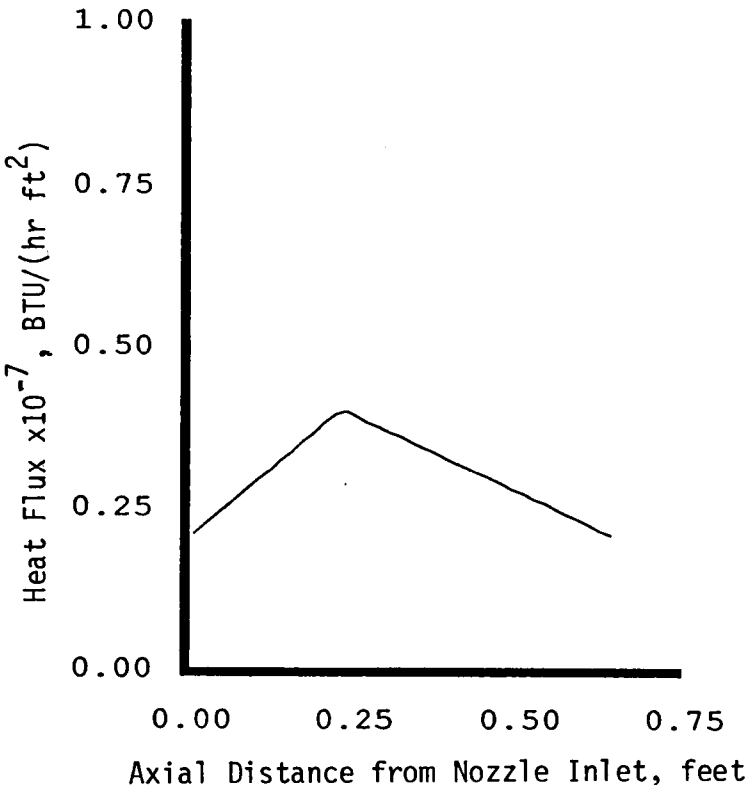


Figure 3.5 Typical Heat Flux Distribution Chosen for Numerical Calculations (Run #35)

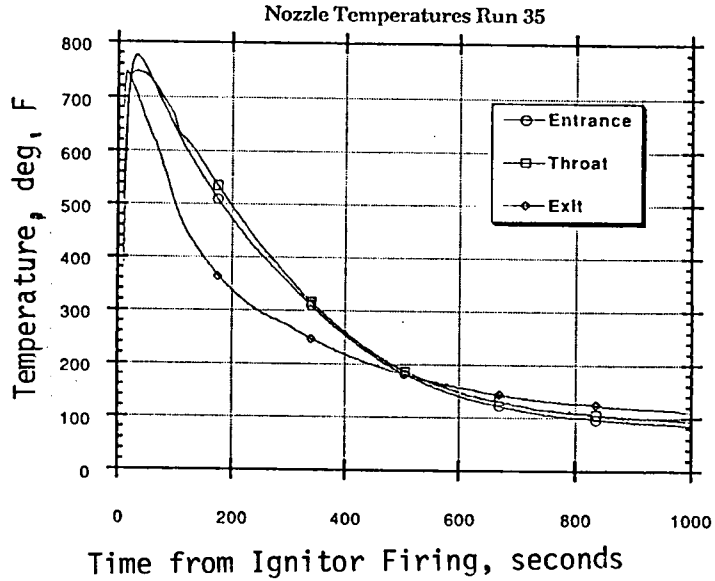


Figure 3.6 Nozzle Temperature Transients for Run #35 over 1000 Seconds Following Ignition

The results of three such calculations, run numbers 28, 32 and 35, are discussed.

Figure 3.7 shows the results for run #35 which was an extended duration firing. Figure 3.7 a) shows the calculated and experimental temperature transients at the nozzle inlet location. It can be seen that the experimental data curve shows a strange behavior between 5 and 6 seconds from ignition. It is probably attributable to some experimental malfunction or an instrument error. Up to that point of time, the comparison is acceptable. Figures 3.7 b) and 3.7 c) show the temperature transients at the throat and exit locations respectively. In both cases, the experimental data compares fairly well with the calculations.

Figure 3.8 shows the comparisons for run #32. The data from the thermocouple at the nozzle back face, an inch from inlet, was bad. The comparisons are again fairly good.

Figures 3.9 shows such plots for run #28. Again in figure 3.9 a), the experimental data shows strange behavior at around 3.0 seconds after ignition, probably due to one of the reasons given with reference to data from run #35. The comparisons are quite favorable.

3.3.2 ERROR ANALYSIS

All the finite difference forms used for spatial derivatives are second order accurate and the finite difference form used for the time derivative is first order accurate. Hence, the scheme is second order accurate in both the spatial dimensions and first order accurate in time. In other words, the truncation error associated with the scheme is of order (δt,δz^2 ,δr^2). As these errors tend to zero as the spatial grid sizes and the time step tend to zero, the scheme is consistent.

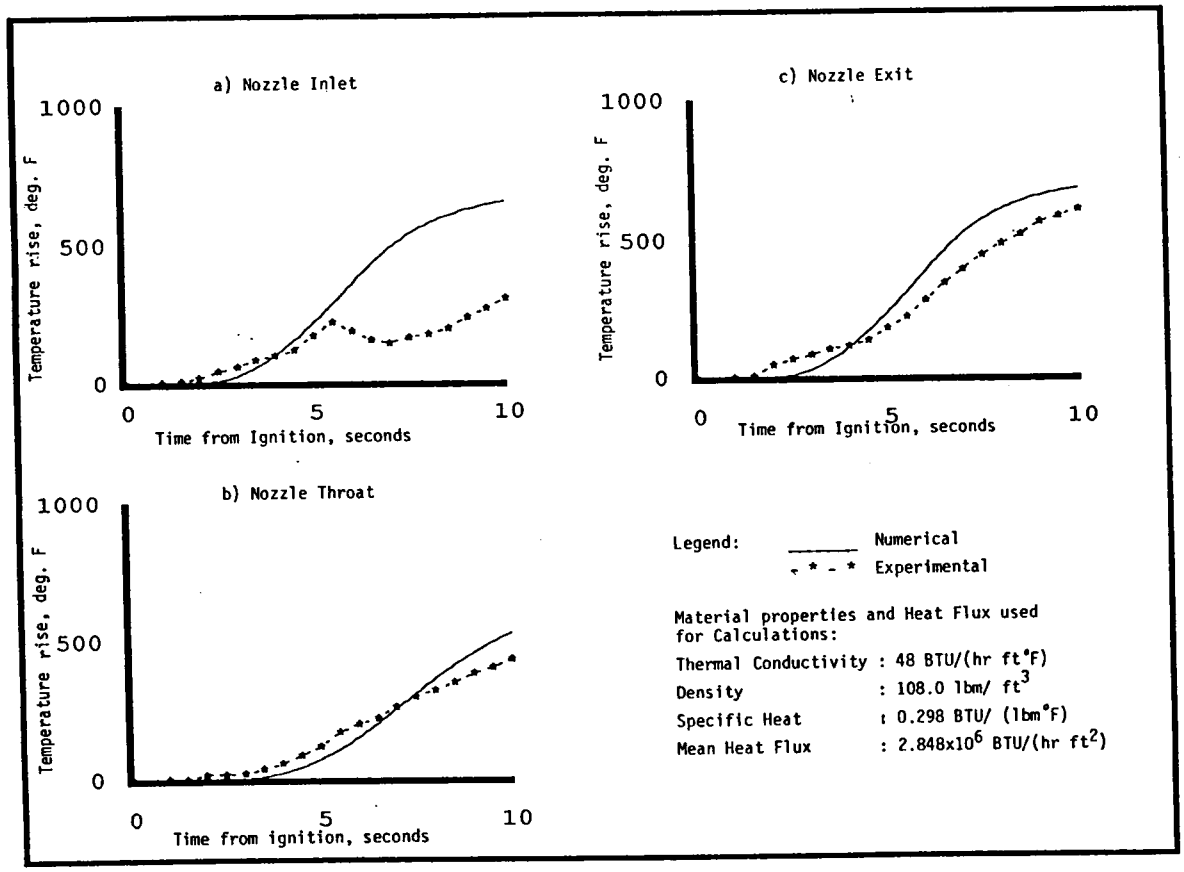


Figure 3.7 Comparison of Numerical and Experimental Temperature Transients, Run #35

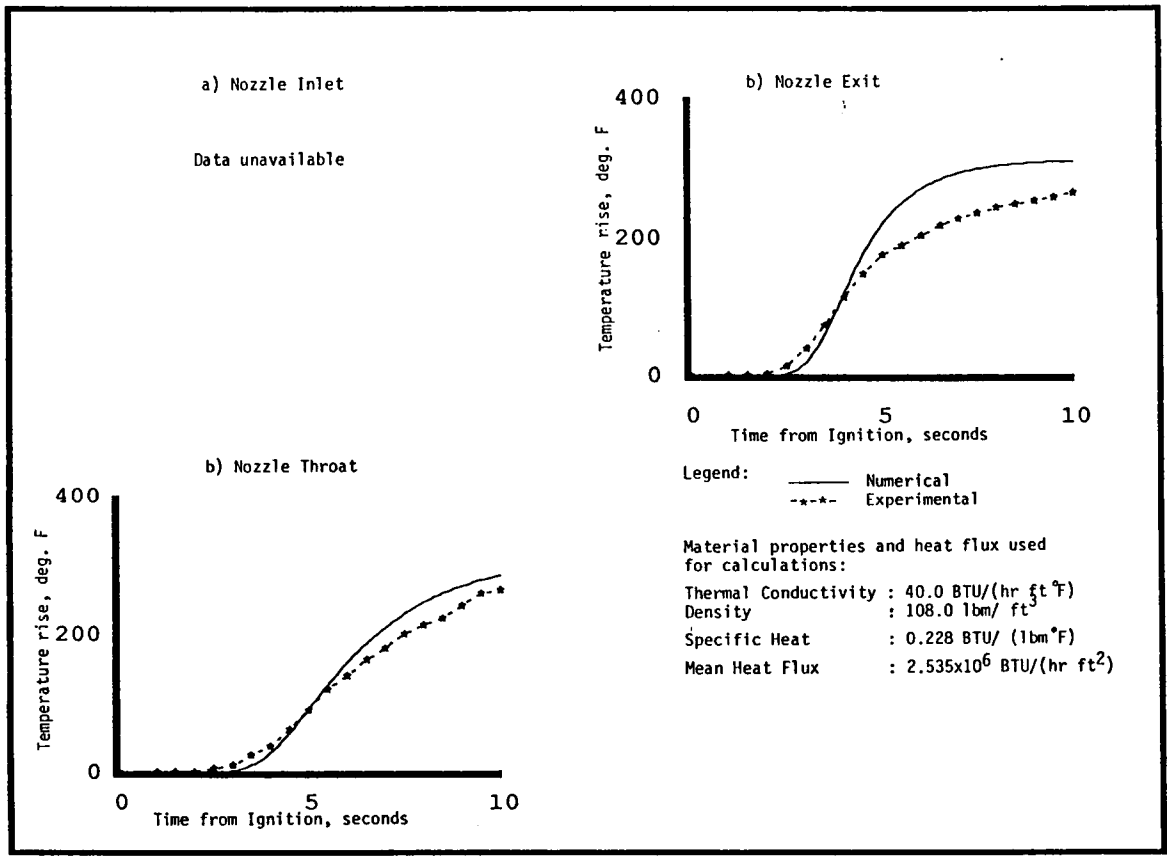


Figure 3.8 Comparison of Numerical and Experimental Temperature Transients, Run #32

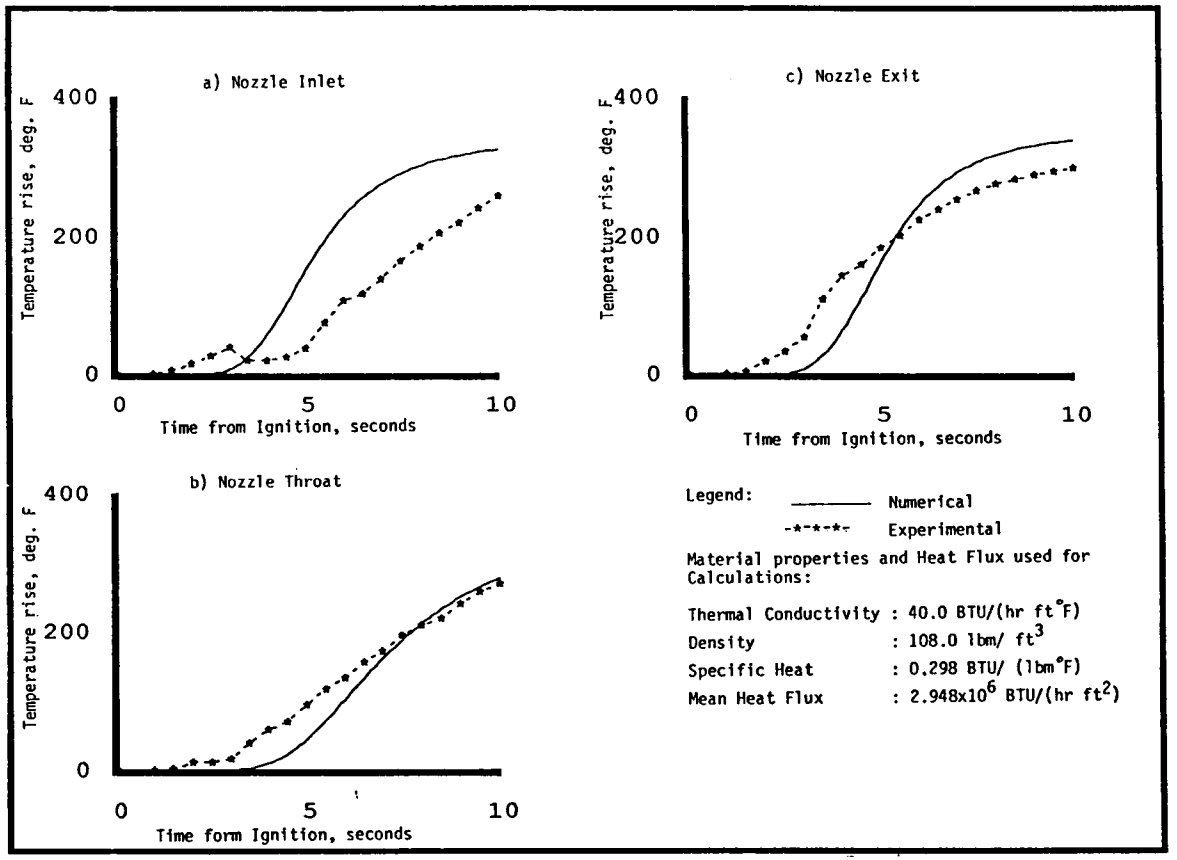


Figure 3.9 Comparison of Numerical and Experimental Temperature Transients, Run #28

Another error that arises is numerical round off errors due to finite digit computations. There are of course errors associated with the experimental instrumentation- to name a few of these, errors in measurement of temperature and time.

The main error check performed on the numerical results was to compare the heat input and the change in heat stored in the nozzle. This essentially checks if the model conserves energy. For all the calculations performed, the magnitude of this error was less than two percent. That is,

$$\left|\frac{\text{Heat input} - \text{Change in Heat stored}}{\text{Heat input}}\right| \leq 0.02$$

Figure 3.10 shows the variation of this error with time for one calculation. As can be seen from this figure, the error always remains between +2 percent and -2 percent. This was true of all calculations. This error, its magnitude being consistently below two percent, is considered acceptable.

3.3.3 EXPLANATIONS FOR DEVIATIONS

Even though every effort has been made to simulate conditions that existed during experiments, unfortunately certain details could not be exactly replicated. Hence, the calculations were not perfect simulations of actual experiments. The following discrepancies between theory and experiment can be identified.

(i) The calculations used assumed constant properties throughout the entire nozzle. In the actual experiment, during the initial heat input period, there is a significant temperature difference between the nozzle inner face and

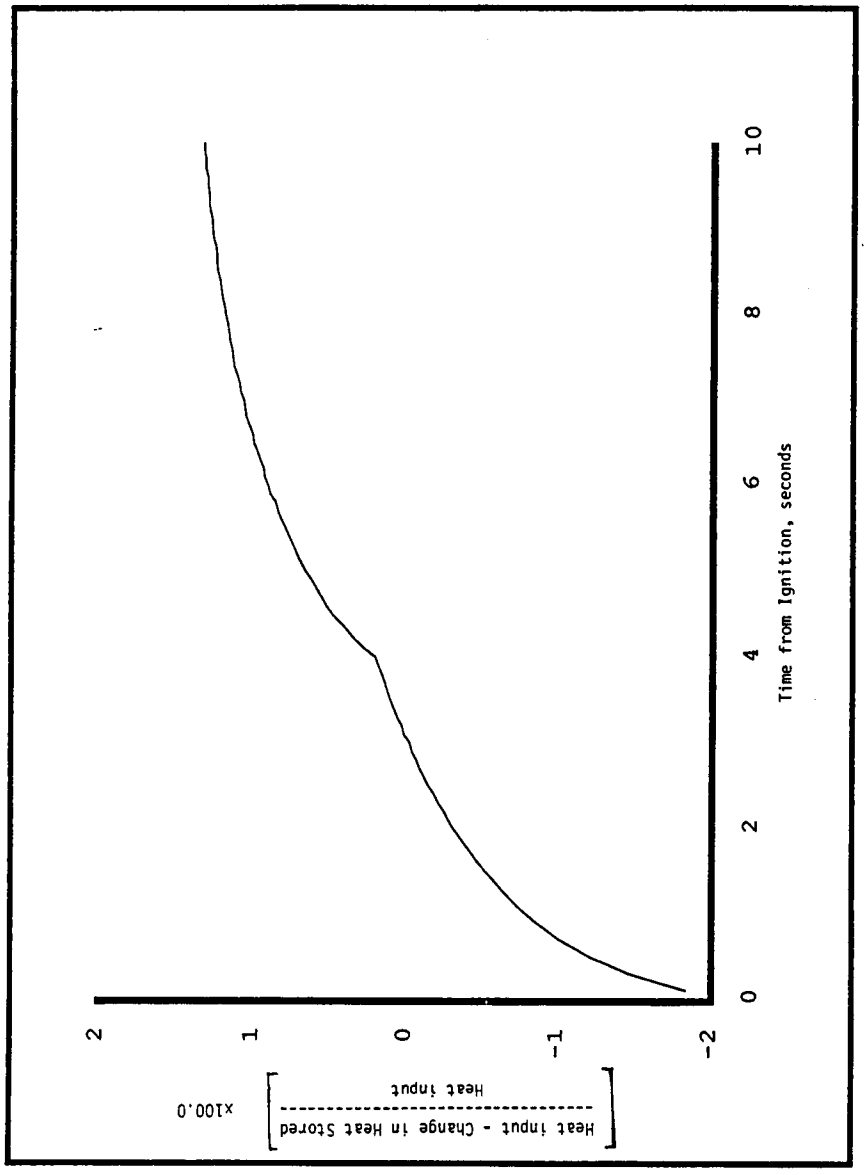


Figure 3.10 Comparison of Heat Input and the Change in Heat Stored, Run #35

the back face. Hence there may a distinct difference in the properties, especially the thermal conductivity, of the material in different parts of the nozzle. This difference, though, vanishes quickly as the temperatures in different regions of the nozzle equilibrate.

(ii) The heat flux distribution shown in figure 3.5, resembles the character of the actual heat flux distribution, but, there is no guarantee that the chosen distribution is exactly the same as that which existed in experiment.

(iii) During the experiments, immediately after the fuel firing, a nitrogen purge cooling is initiated. The cold nitrogen flows past the fuel grain first and then through the nozzle. After firing, the fuel grain will heat the purge nitrogen. As a result, the nitrogen can heat the nozzle for a very short time after the purge initiation. Subsequently, it cools the nozzle. In the numerical calculations, it is assumed that the nozzle inner face is insulated after the combustion terminates.

(iv) It is also assumed that the nozzle back face and the two end faces are perfectly insulated. These faces actually conduct and can exchange some heat to the surroundings, however small the amount might be.

(v) The heat flux during the experiments is quite likely to have varied even over the short firing duration, as for example, as the wall surface temperature rises. However, in the calculations it is assumed that the heat flux remains constant with time during firing and varies only along the length.

3.3.4 NOZZLE INNER FACE TEMPERATURES

The experiments were not instrumented to get temperatures at different

locations in the nozzle except for three points on the back face. The safe operation of the nozzle depends on keeping the critical points in the nozzle within the acceptable temperature limits. The highest temperatures occur on the nozzle inner face, at the end of the heat input period. The temperatures at these points were not measured. The numerical calculations could however estimate these temperature transients. Figure 3.11 shows the transients of temperature at three points on the nozzle inner face. These points are exactly in line with the three thermocouples on the back face. Figure 3.11 corresponds to run #35, the one that had the longest firing period.

It can be seen from this figure that the maximum temperature occurs at the throat on the nozzle inner surface exposed to the plasma. The maximum temperature as predicted for the longest duration firing is 3150 degrees F. This temperature is acceptable from the nozzle material point of view. The nozzle material ATJ Graphite undergoes ablation only at a temperature of 3500 degrees F. Figure 3.11 suggests that there should have been no damage to the nozzle material after the seven firings. This is also confirmed by experiments, where there was only minor noticeable deterioration of the nozzle material, less than 0.001 inch increase in the throat diameter after a run.

These results indicate that the material temperatures remain within the safe limits. As this is the case with the longest firing duration experiment, it can be expected that the same be true of other experiments as well. Table 3.3 gives the estimated maximum temperatures on the nozzle inner surface for other runs. These results imply that there should not have been any large scale erosion or burning of the nozzle inner face. This was confirmed from the experimental observations also.

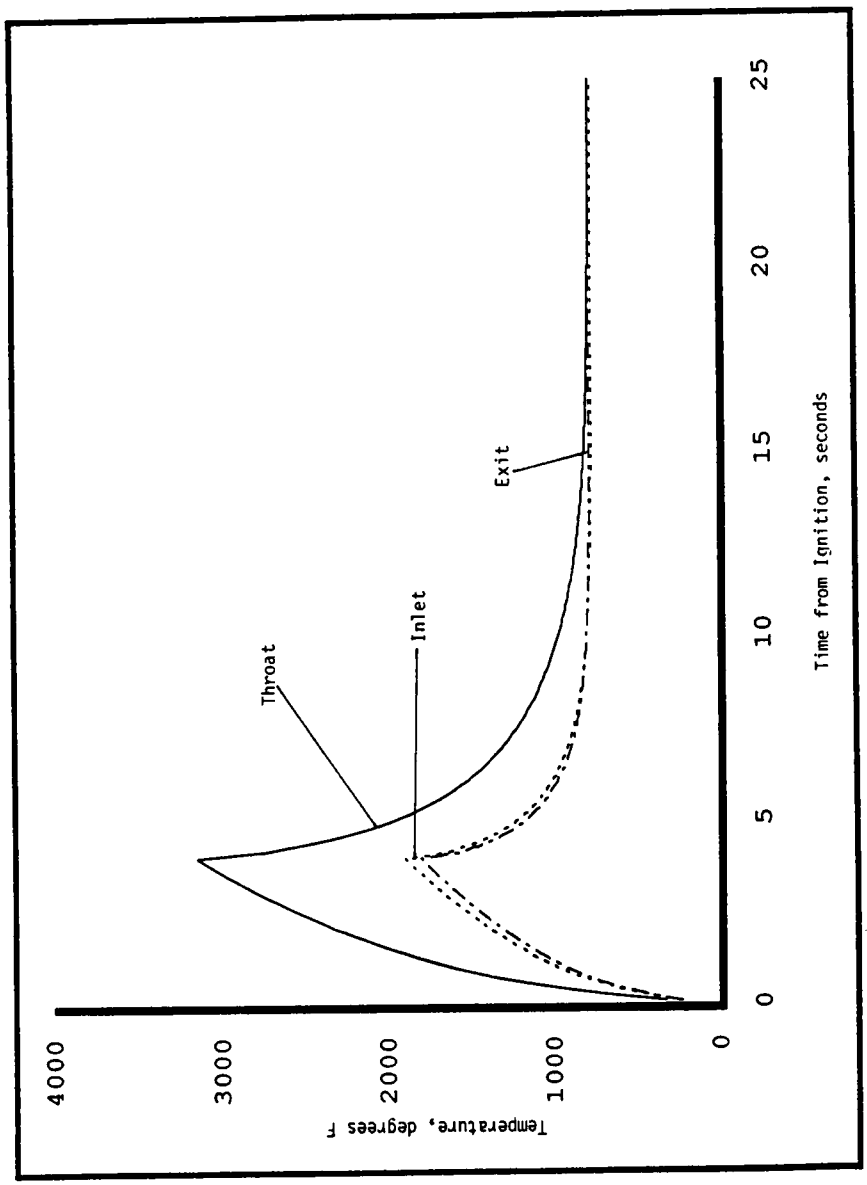


Figure 3.11 Nozzle Inner Face Temperature Transients, Run #35

TABLE 3.3

Estimated Maximum Temperatures on the Nozzle Inner Surface

(Temperatures are in °F)

Run No.	Location		
	Inlet	Throat	Exit
10	1279	2130	1214
20	1279	2130	1214
24	1622	2710	1538
28	1297	2165	1230
32	1277	2133	1211
35	1897	3147	1802

3.3.5 TWO DIMENSIONAL NATURE OF SOLUTIONS

While the experimental data comparison is limited to specific points, the two dimensional character of the numerical solution can be considered as well. To show that the solution of the numerical procedure also reflects this character, which is not clearly evident from the previous figures, the numerical results can be displayed as time wise isotherms in the nozzle block.

Figure 3.12 shows the isotherms at 700 degrees F as they move with time. This figure corresponds to run #35. Besides the movement of isotherm lines towards the nozzle back face, it can also be noticed that the lines bend inwards as they move. It is known that heat conduction is in a direction normal to the isotherms. The isotherms in this figure are not exactly parallel to the nozzle axis. This indicates that besides conduction in the radial direction, conduction occurs in the axial direction also. In fact, the axial conduction is more distinct in the regions near the back face as the isotherms are almost aligned with the radii, indicating that the heat transfer is in the axial direction.

It is also interesting to look at isotherms corresponding to a temperature above the nozzle soak temperature. For run #35, the ideal equilibrium (without nitrogen purge cooling) temperature is 780 degrees F. Figures 3.12 b) and c) show the motion of isotherm lines at 850 degrees F for this calculation. Figure 3.12 a) shows the lines moving towards the nozzle back face until seconds from the ignition. As this temperature is above the equilibrium temperature, the isotherm plot after a sufficiently long time after ignition should not show these lines. This is so because the entire nozzle is at the equilibrium temperature as time tends to infinity. The mechanism by which these lines disappear from the nozzle is evident from figure 3.12 b). The lines retreat towards the nozzle front face and eventually vanish. It is also appropriate to point out that isotherm

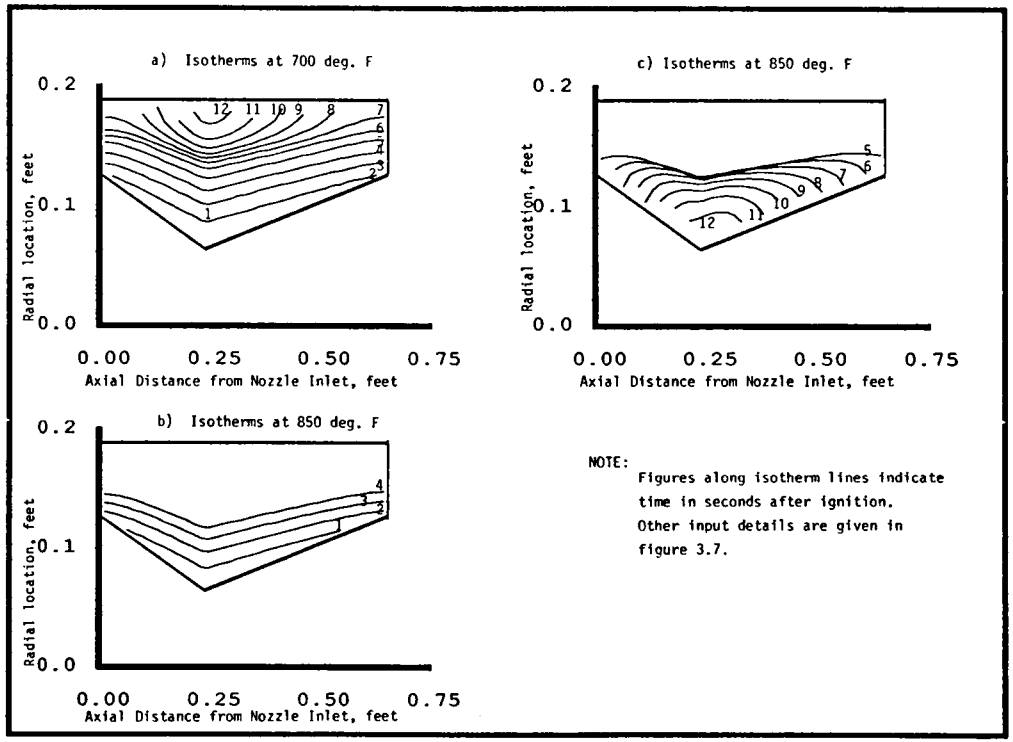


Figure 3.12 Time History of Isotherms in the Nozzle Block, Run #35

lines corresponding to a temperature below the equilibrium temperature are also removed after a sufficiently long time, the only difference being that they disappear out of the nozzle back face. Another fashion in which the isotherms can disappear is by forming closed loops which shrink in size and eventually vanish. It is appropriate to point out that whatever be the mode, the above-equlibrium isotherms disappear closer to the front face and the below-equilibrium ones closer to the back face, at least for this nozzle problem.

This phenomenon is to be expected since the temperature at every point in the entire nozzle is the same, and is in fact equal to the equilibrium temperature after enough time has elapsed. Hence isotherms at any temperature other than the equilibrium temperature can not be a part of the nozzle as time tends to infinity.

CHAPTER 4

CONCLUSIONS

The two dimensional heat transfer in a nozzle has been successfully modeled. The results of this numerical model have been compared with analytical solutions as well as experimental data; the comparisons showed that the results check reasonably well. The numerical calculations also predicted the nozzle inner face temperature transients which could not be obtained from experiments. This character also seemed to concur with experimental experience.

The model has been validated against experiments and can be used for thermal designs of similar components in the future. However, the following improvements could be made to enhance the accuracy of the results:

(i) The temperature variation of material properties could be taken into consideration and appropriate modifications made.

(ii) A more accurate heat flux distribution based on actual flow theories could be incorporated.

(iii) The method could be extended to the case of cyclical heating, in particular, to heating followed by significant cooling.

LIST OF REFERENCES

LIST OF REFERENCES

1. Schmidt, H. J., et al, "An Innovative Demonstration of High Power Density in a Compact MHD Generator", Final Report for Contract No. DE-AC22_87PC79678, UTSI, June, 1990.
2. Kolman, B., and W. F. Trench, "Multivariable Calculus with Linear Algebra and Series", Academic Press, New York, 1970.
3. Rohsenow, W. M., and Hartnett, J. P., "Handbook of Heat Transfer", McGraw Hill Book Co., 1973.

APPENDICES

APPENDIX A

Derivatives in the computational plane

$$\frac{\partial T}{\partial r} = \frac{\partial \xi}{\partial r}\frac{\partial T}{\partial \xi} + \frac{\partial \eta}{\partial r}\frac{\partial T}{\partial \eta}$$

$$\frac{\partial T}{\partial z} = \frac{\partial \xi}{\partial z}\frac{\partial T}{\partial \xi} + \frac{\partial \eta}{\partial z}\frac{\partial T}{\partial \eta}$$

$$\frac{\partial}{\partial r} r \frac{\partial T}{\partial r} = r\frac{\partial^2 T}{\partial r^2} + \frac{\partial T}{\partial r}$$

$$\frac{\partial^2 T}{\partial r^2} = (\frac{\partial \xi}{\partial r})^2 \frac{\partial^2 T}{\partial \xi^2} + (\frac{\partial \eta}{\partial r})^2 \frac{\partial^2 T}{\partial \eta^2} + 2\frac{\partial \eta}{\partial r}\frac{\partial \xi}{\partial r}\frac{\partial^2 T}{\partial \eta \partial \xi} + \frac{\partial^2 \eta}{\partial r^2}\frac{\partial T}{\partial \eta} + \frac{\partial^2 \xi}{\partial r^2}\frac{\partial T}{\partial \xi}$$

$$\frac{\partial^2 T}{\partial z^2} = (\frac{\partial \xi}{\partial z})^2 \frac{\partial^2 T}{\partial \xi^2} + (\frac{\partial \eta}{\partial z})^2 \frac{\partial^2 T}{\partial \eta^2} + 2\frac{\partial \eta}{\partial z}\frac{\partial \xi}{\partial z}\frac{\partial^2 T}{\partial \eta \partial \xi} + \frac{\partial^2 \eta}{\partial z^2}\frac{\partial T}{\partial \eta} + \frac{\partial^2 \xi}{\partial z^2}\frac{\partial T}{\partial \xi}$$

APPENDIX B

Finite difference approximations in the computational plane

at point (i,j) (Refer Figure 2.3)

$$\frac{\partial T}{\partial \xi} = \frac{T_{i+1,j} - T_{i-1,j}}{2(\Delta \xi)}$$

$$\frac{\partial T}{\partial \eta} = \frac{T_{i,j+1} - T_{i,j-1}}{2(\Delta \eta)}$$

$$\frac{\partial^2 T}{\partial \xi^2} = \frac{T_{i+1,j} - 2T_{i,j} + T_{i-1,j}}{(\Delta \xi)^2}$$

$$\frac{\partial^2 T}{\partial \eta^2} = \frac{T_{i,j+1} - 2T_{i,j} + T_{i,j-1}}{(\Delta \eta)^2}$$

Point A:

$$\frac{\partial^2 T}{\partial \eta \partial \xi} = \frac{T_{i+1,j+1} - T_{i+1,j-1} - T_{i-1,j+1} + T_{i-1,j+1}}{4(\Delta \xi)(\Delta \eta)}$$

Point B:

$$\frac{\partial^2 T}{\partial \eta \partial \xi} = -\frac{3(T_{i,j+1} - T_{i,j-1}) - 4(T_{i+1,j+1} - T_{i+1,j-1}) + (T_{i+2,j+1} - T_{i+2,j-1})}{4(\Delta \xi)(\Delta \eta)}$$

Point C:

$$\frac{\partial^2 T}{\partial \eta \partial \xi} = -\frac{3(T_{i+1,j} - T_{i-1,j}) - 4(T_{i+1,j+1} - T_{i-1,j+1}) + (T_{i+1,j+2} - T_{i-1,j+2})}{4(\Delta\xi)(\Delta\eta)}$$

Point D:

$$\frac{\partial^2 T}{\partial \eta \partial \xi} = \frac{3(T_{i,j+1} - T_{i,j-1}) - 4(T_{i-1,j+1} - T_{i-1,j-1}) + (T_{i-2,j+1} - T_{i-2,j-1})}{4(\Delta\xi)(\Delta\eta)}$$

Point E:

$$\frac{\partial^2 T}{\partial \eta \partial \xi} = \frac{3(T_{i+1,j} - T_{i-1,j}) - 4(T_{i+1,j-1} - T_{i-1,j-1}) + (T_{i+1,j-2} - T_{i-1,j-2})}{4(\Delta\xi)(\Delta\eta)}$$

Point F:

$$\frac{\partial^2 T}{\partial \eta \partial \xi} = -[\frac{3(3T_{i,j} - 4T_{i+1,j} + T_{i+2,j}) - 4(3T_{i,j-1} - 4T_{i+1,j-1} + T_{i+2,j-1})}{4(\Delta\xi)(\Delta\eta)}$$

$$+\frac{(3T_{i,j-2} - 4T_{i+1,j-2} + T_{i+2,j-2})}{4(\Delta\xi)(\Delta\eta)}]$$

Point G:

$$\frac{\partial^2 T}{\partial \eta \partial \xi} = [\frac{3(3T_{i,j} - 4T_{i+1,j} + T_{i+2,j}) - 4(3T_{i,j+1} - 4T_{i+1,j+1} + T_{i+2,j+1})}{4(\Delta\xi)(\Delta\eta)}$$

$$+\frac{(3T_{i,j+2} - 4T_{i+1,j+2} + T_{i+2,j+2})}{4(\Delta\xi)(\Delta\eta)}]$$

Point H:

$$\frac{\partial^2 T}{\partial \eta \partial \xi} = -[\frac{3(3T_{i,j} - 4T_{i-1,j} + T_{i-2,j}) - 4(3T_{i,j+1} - 4T_{i-1,j+1} + T_{i-2,j+1})}{4(\Delta\xi)(\Delta\eta)}$$

$$+\frac{(3T_{i,j+2} - 4T_{i-1,j+2} + T_{i-2,j+2})}{4(\Delta\xi)(\Delta\eta)}]$$

Point I:

$$\frac{\partial^2 T}{\partial \eta \partial \xi} = [\frac{3(3T_{i,j} - 4T_{i-1,j} + T_{i-2,j}) - 4(3T_{i,j-1} - 4T_{i-1,j-1} + T_{i-2,j-1})}{4(\Delta\xi)(\Delta\eta)}$$

$$+\frac{(3T_{i,j-2} - 4T_{i-1,j-2} + T_{i-2,j-2})}{4(\Delta\xi)(\Delta\eta)}]$$

APPENDIX C

Finite difference forms of Boundary Conditions

(Point designations are referred to Figure 2.3)

Point B:

$$T_{i-1,j} = T_{i,j} + Z_2 \frac{\Delta\xi}{\Delta\eta} \frac{\partial\eta}{\partial z} \left(\frac{T_{i,j+1} - T_{i,j-1}}{2} \right)$$

Point C:

$$T_{i,j-1} = T_{i,j} + \frac{G_2}{G_1} \frac{\Delta\eta}{\Delta\xi} \left(\frac{T_{i+1,j} - T_{i-1,j}}{2} \right) + \frac{\dot{q}}{k} \frac{\Delta\eta}{G_1}$$

Point D:

$$T_{i+1,j} = T_{i,j} - Z_2 \frac{\Delta\xi}{\Delta\eta} \frac{\partial\eta}{\partial z} \left(\frac{T_{i,j+1} - T_{i,j-1}}{2} \right)$$

Point E:

$$T_{i,j+1} = T_{i,j}$$

Point F:

$$T_{i,j+1} = T_{i,j}$$

$$T_{i-1,j} = T_{i,j} + Z_2 \frac{\Delta\xi}{\Delta\eta} \frac{\partial\eta}{\partial z}(T_{i,j} - T_{i,j-1})$$

Point G:

$$T_{i,j-1} = T_{i,j} + \frac{G_2}{G_1} \frac{\Delta\eta}{\Delta\xi}(T_{i+1,j} - T_{i,j}) + \frac{\dot{q}}{k} \frac{\Delta\eta}{G_1}$$

$$T_{i-1,j} = T_{i,j} + Z_2 \frac{\Delta\xi}{\Delta\eta} \frac{\partial\eta}{\partial z}(T_{i,j+1} - T_{i,j})$$

Point H:

$$T_{i,j-1} = T_{i,j} + \frac{G_2}{G_1} \frac{\Delta\eta}{\Delta\xi}(T_{i,j} - T_{i-1,j}) + \frac{\dot{q}}{k} \frac{\Delta\eta}{G_1}$$

$$T_{i+1,j} = T_{i,j} + Z_2 \frac{\Delta\xi}{\Delta\eta} \frac{\partial\eta}{\partial z}(T_{i,j} - T_{i,j+1})$$

Point I:

$$T_{i,j+1} = T_{i,j}$$

$$T_{i+1,j} = T_{i,j} + Z_2 \frac{\Delta\xi}{\Delta\eta} \frac{\partial\eta}{\partial z}(T_{i,j-1} - T_{i,j})$$

VITA

S. BABU was born on November 25, 1962 in Kumbakonam, Tamilnadu, India. He went through two top high schools, Sainik School in Amaravathinagar and Jawahar School in Neyveli, and then to the eminent P.S.G. College of Technology, Coimbatore, University of Madras. In January, 1985 he graduated with a Bachelor of Engineering degree in Mechanical Engineering.

Mr. Babu worked as a Research Engineer with the Bharat Heavy Electricals Limited(BHEL)- from 1985 to 1988 in their Magnetohydrodynamics Center, Trichy, India. During this period, he published four papers. He joined the University of Tennessee Space Institute (UTSI), Tullahoma, Tennessee in August, 1988. At UTSI, he worked as a Graduate Research Assistant on a United States Department of Energy contract on High Temperature Air Heaters. He has completed all the requirements to graduate in December, 1990 with the Master of Science degree in Mechanical Engineering.